

Modelling of energy harvesting with bendable concrete and surface-mounted PVDF

Xie, Jinbao; Xu, Yading; Wan, Zhi; Ghaderiaram, Ali; Schlangen, Erik; Šavija, Branko

DOI

[10.1088/1361-665X/ad43cb](https://doi.org/10.1088/1361-665X/ad43cb)

Publication date

2024

Document Version

Final published version

Published in

Smart Materials and Structures

Citation (APA)

Xie, J., Xu, Y., Wan, Z., Ghaderiaram, A., Schlangen, E., & Šavija, B. (2024). Modelling of energy harvesting with bendable concrete and surface-mounted PVDF. *Smart Materials and Structures*, 33(8), Article 085008. <https://doi.org/10.1088/1361-665X/ad43cb>

Important note

To cite this publication, please use the final published version (if applicable). Please check the document version above.

Copyright

Other than for strictly personal use, it is not permitted to download, forward or distribute the text or part of it, without the consent of the author(s) and/or copyright holder(s), unless the work is under an open content license such as Creative Commons.

Takedown policy

Please contact us and provide details if you believe this document breaches copyrights. We will remove access to the work immediately and investigate your claim.

PAPER • OPEN ACCESS

Modelling of energy harvesting with bendable concrete and surface-mounted PVDF

To cite this article: Jinbao Xie *et al* 2024 *Smart Mater. Struct.* **33** 085008

View the [article online](#) for updates and enhancements.

You may also like

- [The Performance of Slag Containing Engineered Cementitious Composites](#)
Emad Booya, Adeyemi Adesina, Karla Gorospe et al.
- [Recent studies on the mechanical properties of Engineered Cementitious Composite](#)
Mohammad Khalil Khan, Swagata Nag and Sahil Jaggi
- [Performance of Eco Engineered Cementitious Composites Containing Supplementary Cementitious Materials as a Binder and Recycled Concrete Fines as Fine Aggregate](#)
M R Md Zain, C L Oh and L S Wee

PRIME
PACIFIC RIM MEETING
ON ELECTROCHEMICAL
AND SOLID STATE SCIENCE

HONOLULU, HI
October 6-11, 2024

Joint International Meeting of
The Electrochemical Society of Japan (ECSJ)
The Korean Electrochemical Society (KECS)
The Electrochemical Society (ECS)

Early Registration Deadline:
September 3, 2024

MAKE YOUR PLANS NOW!

Modelling of energy harvesting with bendable concrete and surface-mounted PVDF

Jinbao Xie , Yading Xu* , Zhi Wan, Ali Ghaderiaram, Erik Schlangen and Branko Šavija

Microlab, Faculty of Civil Engineering and Geosciences, Delft University of Technology, Delft 2628CN, The Netherlands

E-mail: y.xu-5@tudelft.nl, J.Xie-1@tudelft.nl, Z.Wan-1@tudelft.nl, A.Ghaderiaram@tudelft.nl, Erik.Schlangen@tudelft.nl and B.Savija@tudelft.nl

Received 22 January 2024

Accepted for publication 25 April 2024

Published 2 July 2024



CrossMark

Abstract

Polyvinyl alcohol fiber reinforced engineered cementitious composite (ECC) using piezoelectric polymer film has attracted significant interest due to its energy harvesting potential. This work provides a theoretical model for evaluating the energy harvesting of bendable ECC using surface-mounted polyvinylidene fluoride (PVDF). In the mechanical part, concrete damage plasticity model based on the explicit dynamic analysis was utilized to simulate the dynamic flexural behavior of ECC beam under different dynamic loading rates. The mechanism of force transfer through the bond layer between the PVDF film and ECC specimen was simulated by a surface-surface sliding friction model wherein the PVDF film was simplified as shell element to reduce computational cost. Then, the electromechanical behavior of the piezoelectric film was simulated by a piezoelectric finite element model. A simplified model was also given for a quick calculation. The theoretical model was verified with the experimentally measured mechanical and electrical results from the literature. Finally, a parametric analysis of the effects of electromechanical parameters on the efficiency of energy harvesting was performed. The verified theoretical model can provide a useful tool for design and optimization of cementitious composite systems for energy harvesting application.

Keywords: energy harvesting, ECC, concrete damage plasticity, PVDF, piezoelectric model

1. Introduction

Energy harvesting is a process of extracting energy from ambient resources (e.g. light, temperature, and mechanical

force) and converting into electrical energy. Many materials and devices with different properties have been used to harvest energy, such as piezoelectric [1, 2], triboelectric [3], thermoelectric [4], electromagnetic [5], photovoltaic [6], or hybrid functional [7] properties. Among them, piezoelectric materials are the most widely implemented because they can harvest abundant energy from mechanical vibrations or deformation. In particular, energy-harvesting from concrete structures has gained a lot of attention in the recent years, as it introduces a powerful, renewable and sustainable way for harvesting mechanical energy in our environment. The harvested energy can be used to effectively power civil structures

* Author to whom any correspondence should be addressed.



Original content from this work may be used under the terms of the [Creative Commons Attribution 4.0 licence](https://creativecommons.org/licenses/by/4.0/). Any further distribution of this work must maintain attribution to the author(s) and the title of the work, journal citation and DOI.

with energy self-sufficiency, which promotes a sustainable and smart infrastructure development.

Piezoelectric transformation occurs when mechanical action (stress and strain) is applied to a polarized piezoelectric material; then, opposite bound charges occur on the surfaces of both ends of the material that are connected to electrodes. When the two electrodes are connected to an electrical power management circuit, the output voltage can be stored as electrical energy for electric power supply. In the past few decades, lead zirconate titanate (PZT) has been the most widely-used piezoelectric ceramic material in many designs of energy harvesters for civil infrastructure and buildings. Many researchers have used PZT piezoceramic disks embedded into pavements to collect the electrical energy from vibration induced by moving vehicle on public roadways [8–11], thereby creating so-called piezoelectric energy harvester (PEH). These PZT-based PEHs have also been further optimized for a power-intensive design, so as to better collect road energy by efficiently utilizing the vehicle load [12]. However, the intrinsic brittleness of the piezoceramic material (PZT) limits its application on curved surfaces and high strain conditions as in the case of civil infrastructure and buildings. Polyvinylidene difluoride (PVDF) is the most popular commercial flexible piezoelectric polymer because it can be easily fabricated as a thin film with large compliance, high ductility, and excellent piezoelectric performance [13]. Considerable research has been dedicated to extracting vibration energy from PVDF transducers using piezoelectric cantilever beam configurations, such as unimorph (a substrate beam with a bonded piezoelectric layer) and bimorph (a substrate beam with two symmetric piezoelectric layers bonded to both sides) devices [14, 15]. Moreover, PVDF shows a strong ability to generate electricity under low-frequency stimuli due to its flexural behavior, which can be flexibly installed in the structure for energy harvesting. In practical applications, PVDF has been widely used in structures exposed to a variety of dynamic loads, e.g. passing vehicles [13], human motions [16–19], sound pressure [20], rain drops and wind [21]. Multiple PVDF films can also be arranged to enhance energy harvesting. Jung *et al* [13] developed a PVDF energy harvester for roadways, rivaling piezoelectric ceramic-based systems. The device, comprising six pre-curved bimorph units aligned vertically, generated 200 mW across a 40 k Ω load resistor in modeled roadway testing in the laboratory.

Application of piezoelectric films for harvesting energy from mechanical deformation of cementitious materials provides a promising approach for civil infrastructure energy self-sufficiency. Cementitious materials are the most widely used construction materials in the world due to their excellent properties and relatively low cost [22]. Moreover, civil structures based on cementitious materials are exposed to a wide range of dynamic loads from vehicles, waves, winds, and human motion, which provides structural deformation or vibrations for energy harvesting through surface-mounted piezoelectric films. Cahill *et al* [23] used PZT and PVDF to harvest energy from train-induced response in RC bridges, which was found to be adequate for powering small wireless

devices for structural health monitoring (SHM). The brittle nature of PZT results in potential reliability risks, and thus flexible PVDF may be a better option for stable energy harvesting. However, the use of PVDF for better energy harvesting requires the host structure to have large deformability and energy dissipation capability. In terms of concrete-like materials, engineered cementitious composite (ECC) is well known for its pseudo strain-hardening behavior and excellent crack control capacity, which can provide high strain energy through large deflections to flexible piezoelectric materials for energy conversion [24]. Su *et al* [25] conducted flexural tests for ECC with surface-mounted PVDF, and its voltage output generated by the PVDF film was synchronously recorded. Their experiments indicate the feasibility and potential of the highly flexible ECC materials attached piezoelectric films for energy harvesting.

Many numerical piezoelectric models have been established for stress and strain monitoring and real-time damage assessment using PZT sensors, which is generally called the electromechanical impedance method [26] for SHM of various civil structures. Simplified piezoelectric models are commonly used to calculate output voltage from PZT patches or PVDF film [17, 27–29]. These simplified formulas regarding piezoelectric effects have been used to calculate the harvesting energy in concrete [23]. However, no known piezoelectric model for energy harvesting was associated with ECC material with surface-mounted piezoelectric films. Some researchers have conducted energy harvesting experiments of cementitious materials by using piezoelectric generator, which is time-consuming and therefore expensive. Numerical modeling can help analyze the mechanical and electrical mechanisms behind experimental observations, and provide a theoretical prediction of energy harvesting potential from cementitious materials in complicated cases. Also, a model-based parametric analysis allows studying the effects of mechanical and electrical parameters on energy harvesting, so as to provide assessment of performances or optimization design for further application.

In this paper, an energy harvesting model was developed to evaluate the electrical energy as a result of the conversion of the mechanical energy of ECC subjected to bending using a surface mounted PVDF film. The flexural behavior of ECC beams under different dynamic loading rates was simulated by concrete damage plasticity (CDP) model. Then, a finite element model (FEM)-based piezoelectric model was proposed to calculate the output voltage generated by the PVDF film. Meanwhile, a simplified piezoelectric model was also given to calculate the output voltage. The simulated results agree well with the experimental measurements in literature regarding mechanical and electrical results. Finally, the effects of electromechanical parameters on the output voltage were examined. The energy harvesting model established in this study is applicable for practical construction applications. This includes the extraction of energy from induced structural deformations or vibrations caused by passing trains in long-span bridges, as well as the harvesting of vibration energy from tuned mass dampers in tall buildings and earthquake-resistant structures.

2. Theoretical modeling

2.1. CDP model

The CDP model [30–32] was adopted for simulating the nonlinear behavior of ECC due to plasticity and damage, which is:

$$\sigma = (1 - d)E_0 (\varepsilon - \varepsilon^{pl}) \quad (1)$$

where σ is the stress; $\varepsilon, \varepsilon^{pl}$ are the total strain and plastic strain, respectively. E_0 represents the initial Young's modulus of ECC. d represents the damage factor used for quantifying stiffness degradation, in a range of 0–1. And it requires that the d increases monotonically with strain. Here, as fiber reinforced cementitious material was used, the stress does not decrease monotonically with strain when the material was loaded in tension. Hence, stiffness degradation was not able to be considered in this chapter.

The following yield criterion in the CDP model is used to describe the initiation of plastic strain

$$F = \frac{1}{1 - \alpha} (\bar{q} - 3\alpha\bar{p} + \beta (\varepsilon^{pl}) (\widehat{\sigma}_{\max}) - \gamma (-\widehat{\sigma}_{\max})) - \widehat{\sigma}_c (\varepsilon_c^{pl}) \quad (2)$$

where

$$\alpha = \frac{(\sigma_{b0}/\sigma_{c0}) - 1}{2(\sigma_{b0}/\sigma_{c0}) - 1} \quad (3)$$

$$\beta = \frac{\bar{\sigma}_c (\varepsilon_c^{pl})}{\bar{\sigma}_t (\varepsilon_t^{pl}) - 1} (1 - \alpha) - (1 + \alpha) \quad (4)$$

$$\gamma = \frac{3(1 - K_c)}{2K_c - 1} \quad (5)$$

where \bar{p} represents the effective hydrostatic pressure. \bar{q} represents the von Mises equivalent effective stress. The subscripts 't' and 'c' represent tension and compression, respectively. $\widehat{\sigma}_{\max}$ refers to the maximum principal effective stress. σ_{b0}/σ_{c0} refers to the ratio of initial equi-biaxial and initial uniaxial compressive yield stress, which takes a default value of 1.16 in ABAQUS. K_c describes the ratio of second stress invariants on tensile and compressive meridians for a given invariant \bar{p} , which takes a default value of 1.16 in ABAQUS.

Assuming non-associated potential plastic flow in the CDP model, the flow potential G based on the Drucker–Prager hyperbolic function takes the form

$$G = \sqrt{(\varepsilon_{ec}\sigma_{t0}\tan\psi)^2 + \bar{q}^2} - \bar{p}\tan\psi \quad (6)$$

where ψ is the dilation angle. σ_{t0} is the uniaxial tensile stress at failure. ε_{ec} is the eccentricity that defines the rate at which the function approaches the asymptote, which generally takes a value of 0.1 in ABAQUS.

According to Zhou *et al* [33], the constitutive relationship of ECC can be simplified, as shown in figure 1. Herein,

its compressive model (figure 1(a)) can be represented by equation (7)

$$\sigma_c = \begin{cases} E_0\varepsilon & 0 < \varepsilon \leq \varepsilon_{0.4} \\ E_0\varepsilon(1 - \alpha) & \varepsilon_{0.4} < \varepsilon \leq \varepsilon_0 \\ m(\varepsilon - \varepsilon_0) + f'_{cr} & \varepsilon_0 < \varepsilon \leq \varepsilon_l \\ n(\varepsilon - \varepsilon_0) + \sigma_l & \varepsilon_l < \varepsilon \leq \varepsilon_{\max} \end{cases} \quad (7)$$

where ε_0 refers to the strain at the peak load. $\varepsilon_{0.4}$ refers to the strain at 40% of the peak load. f'_{cr} represents the stress at the peak load. m, n determine the slope of the bilinear curve, which can be calibrated by experiments. σ_l, ε_l represent the stress and strain at the inflection point, respectively. α refers to the reduction factor for elastic modulus, which is calculated as follows

$$\alpha = a \frac{E_0\varepsilon}{f'_{cr}} - b \quad (8)$$

where a and b can be obtained according to the slope of the equivalent hardening line.

As indicated in figure 1(b), the tensile behavior of ECC can be simplified by a trilinear curve, which can be described by equation (9) [34]. Herein, the second part of the curve ($\varepsilon_{t0} < \varepsilon \leq \varepsilon_{tp}$) is employed to model the tension stiffening characteristics of ECC. $\sigma_{t0}, \sigma_{tp}, \varepsilon_{t0}, \varepsilon_{tp}$ can be used to modify the tension stiffening behavior of ECC according to the experimental tensile data

$$\sigma_t = \begin{cases} E_0\varepsilon & 0 < \varepsilon \leq \varepsilon_{t0} \\ \sigma_{t0} + (\sigma_{tp} - \sigma_{t0}) \left(\frac{\varepsilon - \varepsilon_{t0}}{\varepsilon_{tp} - \varepsilon_{t0}} \right) & \varepsilon_{t0} < \varepsilon \leq \varepsilon_{tp} \\ \sigma_{tp} \left(1 - \frac{\varepsilon - \varepsilon_{tp}}{\varepsilon_{tu} - \varepsilon_{tp}} \right) & \varepsilon_{tp} < \varepsilon \leq \varepsilon_{tu} \\ 0 & 0 \end{cases} \quad (9)$$

2.2. Interaction between ECC and piezoelectric polymer

In general, piezoelectric patches or polymers wrapped with a protective cover are surface bonded to the host structure by using adhesives. Previous studies have indicated that a surface-mounted piezoelectric patch is not perfectly bonded with the host structure during its deformation process (including patch debonding, patch breakage/scratch, and patch detaching [35, 36]), which has significant impacts on the output voltage [37]. Figure 2 presents the mechanism for the interaction between the host structure and the piezoelectric polymer. Herein, '1' represents the axial direction, '3' represents the vertical direction. As indicated in figure 2(a), there is a bond layer between the host structure and the piezoelectric polymer, which limits the separation of the two in the normal direction. In the tangential direction, the relative movement of the two is limited by corresponding adhesive friction (τ) that occurs at the interface between the host structure and the bond layer, as well as the interface between the bond layer and the piezoelectric polymer. However, it should be noted that the bond layer deforms unevenly due to the shear lag effect [38, 39], which results in relative slip between the host structure and the piezoelectric polymer, as shown in figure 2(b). Herein, u_p is the deformed position of the interface between the bond layer and the host

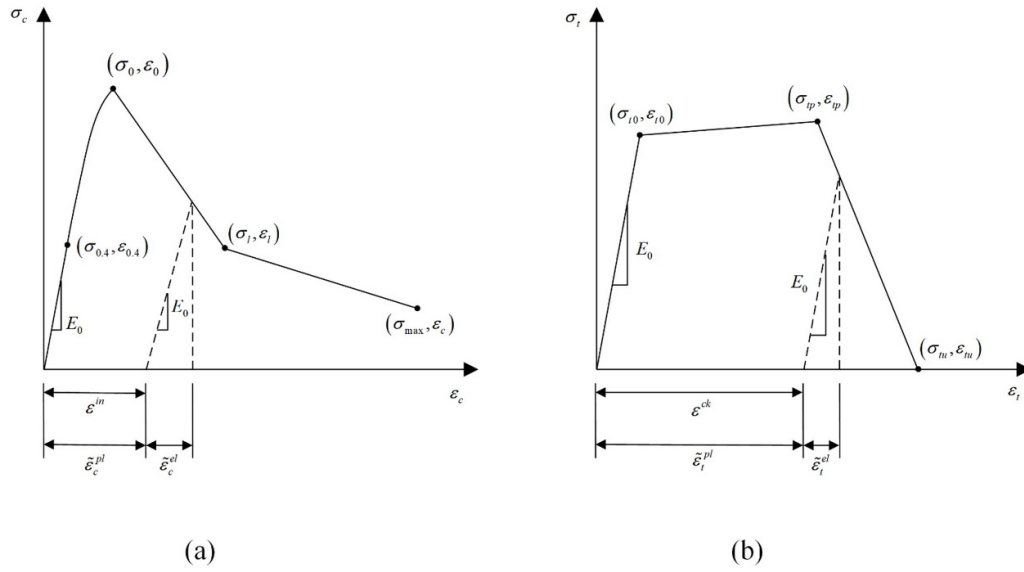


Figure 1. Constitution of the CDP model for ECC: (a) compression; (b) tension.

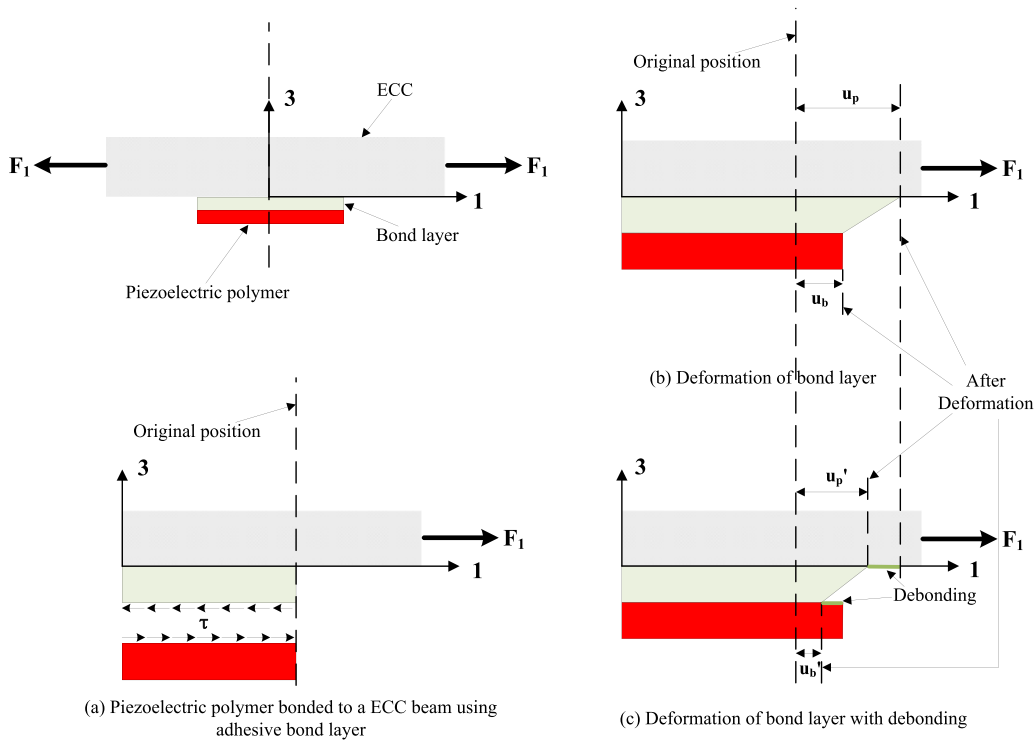


Figure 2. Interaction between the host structure and the piezoelectric polymer using adhesive bond layer.

structure. u_b is the deformed position of the interface between the bond layer and the piezoelectric polymer. Generally, if debonding occurs on these interfaces during the deformation process (especially in the bending case), u_p will reduce to u_p' , u_b will reduce to u_b' , as shown in figure 2(c). These effects inevitably cause a difference in deformation between the piezoelectric polymer and the associated host structure surface.

Compared to the host structure, the adhesive layer has a negligible mass and stiffness, and is thus omitted from the mechanical simulation [39]. Then, for the force transmission

of the adhesive layer, the piezoelectric polymer and the host structure are exposed to the adhesive friction from the bond layer, which can be simplified by a surface-surface friction model. To be specific, the bottom surface of the host structure is the master surface, and the top surface of the piezoelectric polymer is the slave surface. A sliding friction model with a friction coefficient is considered for the two surfaces in the tangential direction. In the normal direction, the slave surface is not allowed to detach from the master surface, and there is also no overclosure between the two surfaces, which means

the slave surface does not penetrate the master surface. In this way, the strain difference between the piezoelectric polymer and the associated host structure surface induced by the bonding condition can be reflected in the model.

2.3. Piezoelectric model for piezoelectric polymer

2.3.1. FE model for a piezoelectric element. The constitutive equations for the mechanical–electric field coupling effect in a piezoelectric material can be formulated as [27]:

$$\begin{aligned} S_{ij} &= s_{ijkl}^E \cdot T_{kl} + d_{kij} \cdot E_k \\ D_j &= d_{jkl} \cdot T_{kl} + e_{jk}^T \cdot E_k \end{aligned} \quad (10)$$

where D_j is the electric displacement. E_k is the electric field. S_{ij} is the mechanical strain. T_{kl} is the mechanical stress. d_{kij} and d_{jkl} refer to the piezoelectric strain coefficients. s_{ijkl}^E represents the mechanical compliance measured at constant electric field. e_{jk}^T refers to the dielectric permittivity measured at constant stress. The superscripts ‘E’ and ‘T’ represent that this quantity is measured at constant electric field and constant mechanical stress, respectively. For d_{kij} and d_{jkl} , the first subscript indicates the direction of the electric field, and the second and third subscripts together indicate the direction of the associated mechanical stress.

The tensor form of equation (10) can be written as:

$$\begin{bmatrix} \mathbf{S} \\ \mathbf{D} \end{bmatrix} = \begin{bmatrix} \mathbf{s}^E & -\mathbf{d}^t \\ \mathbf{d} & \mathbf{e}^T \end{bmatrix} \begin{bmatrix} \mathbf{T} \\ \mathbf{E}_{el} \end{bmatrix} \quad (11)$$

where \mathbf{S} is the strain tensor. \mathbf{D} is the electrical displacement vector. \mathbf{T} is the stress tensor. \mathbf{E}_{el} is the electrical field vector. The superscripts ‘E’ and ‘T’ represent that this quantity is measured at constant electric field and constant mechanical stress respectively. \mathbf{s}^E is the compliance tensor measured at constant electric field. \mathbf{e}^T is the dielectric permittivity tensor measured at constant stress. \mathbf{d} is piezoelectric strain tensor. The superscript ‘t’ represents the transpose matrix of this quantity. \mathbf{d}^t is the transpose matrix of \mathbf{d} .

Similarly, equation (10) can be applied to a PVDF film under identical stress conditions. However, in scenarios involving uneven stress, such as in the bending case discussed in this paper, the PVDF film must be subdivided into numerous small rectangular elements. Each rectangular element can then utilize equation (10) as its constitutive equation. A piezoelectric element has both the mechanical degrees of freedom (the displacement vector δ) and the electrical degrees of freedom (the electric potential array ϕ), which can be used to calculate \mathbf{S} and \mathbf{E}_{el} :

$$\begin{bmatrix} \mathbf{S} \\ \mathbf{E}_{el} \end{bmatrix} = \begin{bmatrix} \mathbf{B}_u & 0 \\ 0 & \mathbf{B}_\phi \end{bmatrix} \begin{bmatrix} \delta \\ \phi \end{bmatrix} \quad (12)$$

$$\mathbf{B}_u = \nabla N_u \quad (13)$$

$$\mathbf{B}_\phi = \nabla N_\phi \quad (14)$$

where N_u, N_ϕ are shape functions in terms of displacement and electric potential, respectively. \mathbf{B}_u is the strain-displacement matrix containing the derivatives of N_u ; \mathbf{B}_ϕ is the

electrical field–electric potential matrix containing the derivatives of N_ϕ .

Based on Hamilton’s principle, the governing FE dynamic equations for a piezoelectric finite element can be derived as

$$\begin{aligned} & \begin{bmatrix} \mathbf{m}_{uu} & 0 \\ 0 & 0 \end{bmatrix} \begin{Bmatrix} \hat{u} \\ \hat{\phi} \end{Bmatrix}_e + \begin{bmatrix} \mathbf{c}_{uu} & 0 \\ 0 & 0 \end{bmatrix} \begin{Bmatrix} \hat{u} \\ \hat{\phi} \end{Bmatrix}_e \\ & + \begin{bmatrix} \mathbf{k}_{uu} & \mathbf{k}_{u\phi} \\ \mathbf{k}_{u\phi}^t & \mathbf{k}_{\phi\phi} \end{bmatrix} \begin{Bmatrix} \hat{u} \\ \hat{\phi} \end{Bmatrix}_e = \begin{Bmatrix} f^{\text{ext}} \\ q^{\text{ext}} \end{Bmatrix}_e \end{aligned} \quad (15)$$

where the subscript ‘e’ indicates element quantities. $\hat{u}, \hat{u}, \hat{u}$ represent vectors of nodal displacement, velocity, and acceleration, respectively. $\hat{\phi}, \hat{\phi}, \hat{\phi}$ represent the electric potential, the first derivative of the electric potential, and the second derivative of the electric potential, respectively. f^{ext} is the external force. q^{ext} is the external point charge.

Mechanical stiffness matrix of an element e (dV represents the differential volume) is given as:

$$\mathbf{k}_{uu} = \iiint \mathbf{B}_u^t \mathbf{c}^E \mathbf{B}_u dV. \quad (16)$$

Mass matrix of an element e is:

$$\mathbf{m}_{uu} = \iiint \rho N_u^t N_u dV. \quad (17)$$

Mechanical damping matrix of an element e is:

$$\mathbf{c}_{uu} = \alpha \iiint \rho N_u^t N_u dV + \beta \iiint \mathbf{B}_u^t \mathbf{c}^E \mathbf{B}_u dV. \quad (18)$$

Dielectric stiffness matrix of an element e is given as:

$$\mathbf{k}_{\phi\phi} = \iiint \mathbf{B}_\phi^t \boldsymbol{\epsilon}^S \mathbf{B}_\phi dV. \quad (19)$$

Piezoelectric coupling matrix of an element e is:

$$\mathbf{k}_{u\phi} = \iiint \mathbf{B}_u^t \mathbf{e}^T \mathbf{B}_\phi dV. \quad (20)$$

The global governing equation for all piezoelectric elements can be assembled as:

$$\mathbf{M}_{uu} \ddot{\mathbf{u}} + \mathbf{D}_{uu} \dot{\mathbf{u}} + \mathbf{K}_{uu} \mathbf{u} + \mathbf{K}_{u\phi} \boldsymbol{\varphi} = \mathbf{F} \quad (21)$$

$$\mathbf{K}_{u\phi}^t \mathbf{u} + \mathbf{K}_{\phi\phi} \boldsymbol{\varphi} = \mathbf{Q} \quad (22)$$

where $\ddot{\mathbf{u}}, \dot{\mathbf{u}}, \mathbf{u}, \boldsymbol{\varphi}$ are the global degrees of freedom at nodes. $\mathbf{M}_{uu}, \mathbf{D}_{uu}, \mathbf{K}_{uu}, \mathbf{K}_{u\phi}, \mathbf{K}_{\phi\phi}, \mathbf{F}, \mathbf{Q}$ are the globally assembled quantities for the mechanical mass matrix, the mechanical damping matrix, the mechanical stiffness matrix, the piezoelectric coupling matrix, the dielectric stiffness matrix, the external force, and the external point charge, respectively.

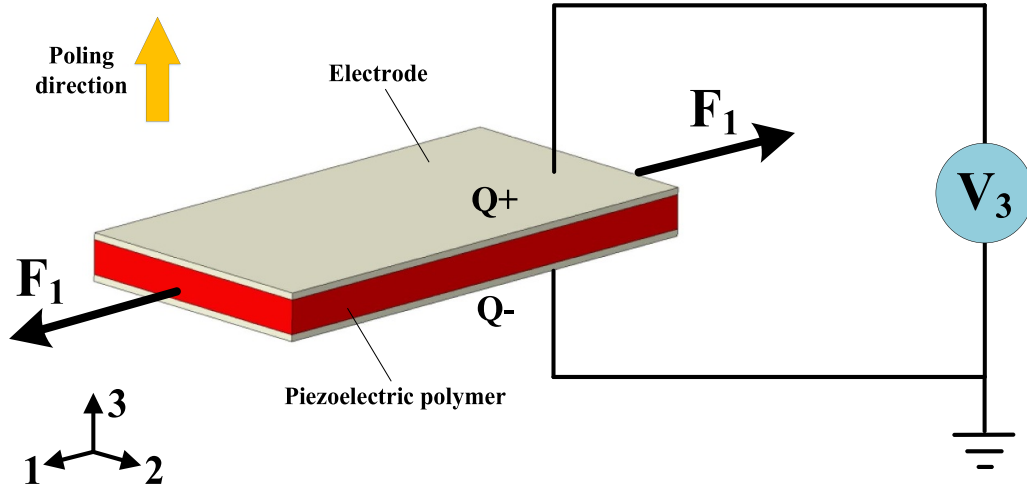


Figure 3. Schematic representation of a piezoelectric film with a d_{31} -coupling mode.

2.3.2. Simplified model. In general, there exist difficult interactions between the ECC specimen and the piezoelectric polymer with complex boundary conditions, making it difficult to model. Therefore, a simplified method needs to be developed for calculating the output voltage. The electrodes of a piezoelectric film are only installed in the plane perpendicular to the direction 3 (figure 3), thus $D_1 = D_2 = 0$. When the piezoelectric film is used as a sensor to measure the mechanical strain for the output voltage, no external electric field is applied. Hence, the electric displacement D_3 in equation (10) can be simply obtained as

$$D_3 = d_{31}\sigma_1 + d_{32}\sigma_2 + d_{33}\sigma_3. \quad (23)$$

For the PVDF film, d_{32} is 10 times smaller than d_{31} or d_{33} , which can be discarded in equation (23) for calculating D_3 generated in the direction 3 [17]. Combined with geometric parameters of the piezoelectric film, equation (23) can be rewritten in equation (24) as the superposition of the two charge generation modes: mode 31 and mode 33 [40, 41].

$$q_3 = d_{31}F_1l_p/t_p + d_{33}F_3 \quad (24)$$

where q_3 is the generated charge in the direction 3. F_1 is the axial force (i.e. in the direction (1) applied in the PVDF film. F_3 is the longitudinal force (i.e. in the direction 3) applied in the PVDF film. l_p , w_p , t_p are the length, width and thickness of the piezoelectric film, respectively.

As indicated in figure 3, when an axial force is applied on the piezoelectric film along the direction 1, the voltage occurs in the two electrodes (i.e. the direction 3), which is generally called d_{31} -coupling mode (mode 31) for voltage generation. Similarly, d_{33} -coupling mode (mode 33) indicates that the voltage generated in the direction 3 is from the force applied in the direction 3.

Generally, a thin PVDF film has a very small thickness (micrometer range), and thus the ratio of l_p/t_p is on the order of 1000. Assuming the same mechanical energy input ($F_1 = F_3$),

the charge generated in mode 31 is about 700 times greater than that in mode 33 (see equation (24)) [17]. For simplicity, the charge generated can be calculated with a d_{31} -coupling mode based on the axial strain of the piezoelectric film

$$q_3 = d_{31}F_1l_p/t_p. \quad (25)$$

As illustrated in figure 3, the top and bottom surfaces of a piezoelectric film are electrodes with a vertical poling direction (i.e. direction 3). The electrode makes the corresponding surface of the piezoelectric film become an equipotential surface, which indicates that all nodes in the surface have the same electric potential. For the entire piezoelectric film, the FE-based piezoelectric model can be simplified to calculate its average strain. The average strain of the piezoelectric film can be calculated as [28]:

$$\varepsilon_{ave} = \frac{1}{V_{tot}} \sum_{j=1}^{N_{el}} \left[\frac{1}{N_{no}} \sum_{i=1}^{N_{no}} \varepsilon_i^j \right] \Delta V_j \quad (26)$$

where ε_i^j is the strain at node i belonging to the volume of element j located on a subvolume of the piezoelectric film. N_{no} is the number of nodes which belong to the related element volume. ΔV_j is the volume of element j located on a subvolume of the piezoelectric film. N_{el} is the number of elements which belongs to the piezoelectric film. V_{tot} is the total volume of the piezoelectric film.

The voltage generated in d_{31} -coupling mode can be calculated by the piezoelectric strain constant d_{31} as indicated in equations (27) and (28) [29]. Herein, the capacitance C_p of the piezoelectric film can be obtained as:

$$C_p = \frac{\varepsilon_{33}l_pw_p}{t_p} \quad (27)$$

where ε_{33} is the 3rd-directional dielectric constant of the piezoelectric film.

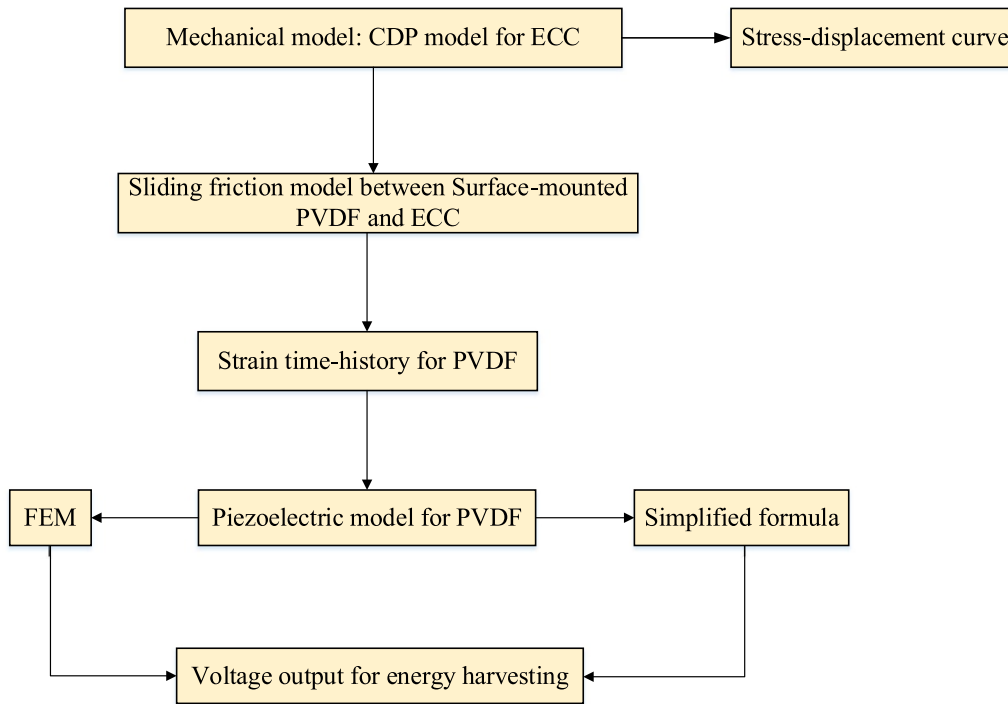


Figure 4. Flowchart of the energy harvesting model of ECC using surface-mounted PVDF.

Then, based on equation (25), the voltage generated can be determined as follows

$$V_p = \frac{d_{31} E_p l_p w_p}{C_p} \varepsilon_{ave} \quad (28)$$

where E_p is the Young's modulus of the piezoelectric film.

2.4. Overview

The output voltage was used as an indicator of the harvesting energy from fiber reinforced cementitious materials. Figure 4 shows the schematical representation and flowchart of an energy harvesting model for evaluating the output voltage of polyvinyl alcohol fiber reinforced ECC (PVA-ECC) with surface-mounted PVDF, which includes the CDP model for mechanical analysis, the interaction between PVA-ECC specimen and PVDF, and the piezoelectric model of PVDF (including FEM and a simplified formula) for calculating the output voltage.

3. Model validation

3.1. Experiment setup

The experimental data from the literature [25] was used to validate the model in this study. In the experiment, a four-point bending test was implemented to study the dynamic flexural behavior of the ECC, as indicated in figure 5. The ECC specimen has a load span of 50 mm (one third of the support span 150 mm). A PVDF film was externally bonded to the underside surface of the ECC specimen at the mid-span. Lead attachment of the PVDF film was accomplished using riveted lugs

connected with 28 AWG wire. The PVDF film has an area of 73 mm × 16 mm with a thickness of 40 μm. As indicated by the manufacturer, the PVDF film is generally laminated to a 0.125 mm polyester substrate as a protective layer. This protective layer made of thin polyurethane can prevent surface oxidation of the silver ink electrode area [25, 42]. Thus, the total thickness of the PVDF film in the mechanical model is taken as 0.165 mm. Displacement control was adopted for the ECC specimen with three different loading rates of 0.5, 1.0, 2.0 mm s⁻¹. During the flexural test, a voltage data logger with the terminal board was used to simultaneously record the output voltage from the PVDF film per millisecond.

Table 1 gives the mixture proportions of ECC by relative weight in terms of cement. Herein Type I Ordinary Portland cement, class C fly ash, silica sand with the maximum particle size of 0.2 mm were used for ECC. PVA fiber has a diameter of 39 μm and a length of 8 mm. The complete mix design is given in table 2.

3.2. Mechanical model based on CDPM

The ABAQUS/explicit module was used for the bending analysis of three-dimensional (3D) ECC with a surface-mounted PVDF film during the dynamic loading process. As shown in figure 6(a), the ECC specimen has a size of 210 mm × 60 mm × 25.4 mm based on the actual geometry of the experimental setup. Dynamic velocity was applied on the top surfaces of the two steel bars located on the top surface of the specimen. Simply supported boundary conditions were adopted for the two steel bars located on the bottom surface of the specimen. To ensure continuous force transmission, tied constraints were used in the interactions between steel bar

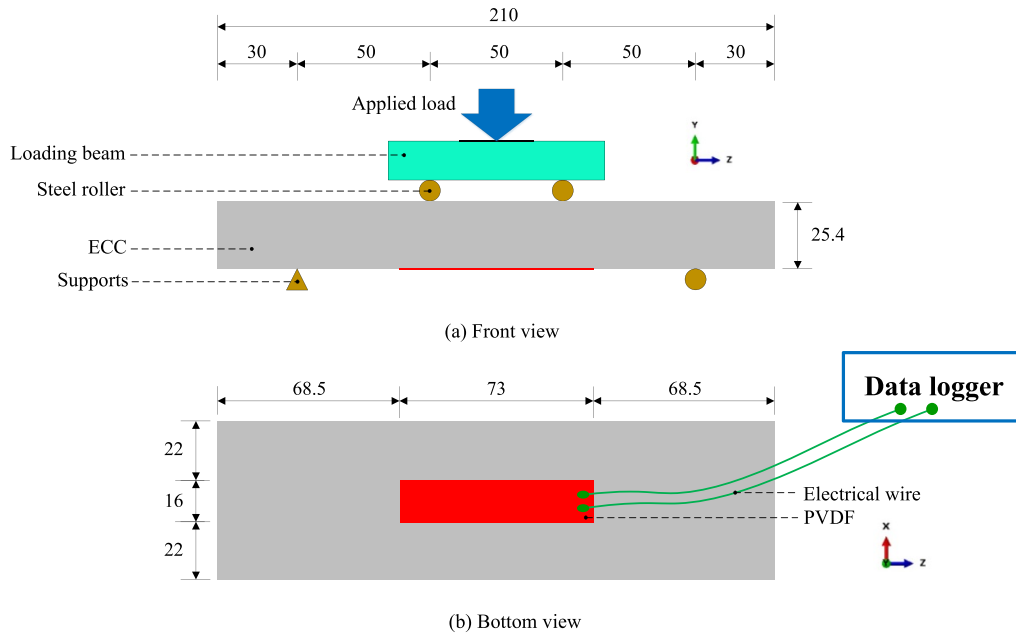


Figure 5. Experiment setup for 4-point bending test (unit: mm).

Table 1. Mixture proportions (by relative weight in terms of cement) [25].

Type	Cement	Fly ash	Silica sand	water	Superplasticizer	PVA fiber (by volume)
PVA-ECC	1.0	1.2	0.8	0.5	0.008	2.0%

Table 2. Material properties of PVA fiber [25].

Type	Diameter (μm)	Length (mm)	Tensile strength (MPa)	Elastic modulus (GPa)	Specific gravity
RECS-15	39	8	1600	41	1.3

and ECC. The ECC specimen and steel bars are all meshed by C3D8R (the eight-node linear hexahedral solid element with reduced integration) in Abaqus. The CDP model parameters for ECC [24, 25, 34] are listed in table 3. ρ_{ECC} refers to the density of ECC. ν_{ECC} refers to Poisson's ratio of ECC. For small strains, however, the material of the PVDF film is considered mechanically isotropic [29]. The elastic modulus, Poisson's ratio of steel are 198.0 GPa, 0.3, respectively. The steel density is 7900 kg m^{-3} .

The stress-strain relationship of the ECC under compression and tension in CDP model were taken based on its experimental results of uniaxial compression and tension tests from the literature [33, 34, 43]. In figure 7 and table 5, Case 1 corresponds to a loading rate of 0.5 mm s^{-1} , Case 2– 1.0 mm s^{-1} , and Case 3– 2.0 mm s^{-1} . As known, the 4-point bending test of ECC is mainly determined by the tensile behavior of the material model. Thus, the compressive behavior parameters are taken based on the experimental values for all cases. The tensile behavior parameters are obtained by several iterations to get a best fitting of the experimental stress–displacement curve using a numerical model. The energy harvesting model specifically targets the pre-peak stress–displacement curve, excluding the portion after the peak stress where failure

occurs, as this segment is crucial for practical engineering applications. This is because that the damage generally occurs after the peak point of the flexural stress (i.e. the softening range) [44, 45], leading to subsequent failure and rendering energy harvesting unsustainable. For the material parameters of CDP model in ECC, compressive behavior parameters are listed in table 4, and tensile behavior parameters in table 5. In the CDP model, the cracking strain is employed to characterize the tensile behavior of ECC after the yield strain occurs. During a tensile test, it is calculated by subtracting the elastic strain corresponding to the undamaged material from the total strain. In plain concrete, cracking usually occurs after the first inflection point, indicating the completion of the elastic phase and the transition into the softening phase accompanied by damage. In ECC, the second part of the curve ($\varepsilon_{10} < \varepsilon \leq \varepsilon_{tp}$) in figure 1(b) is employed to model its tension stiffening characteristics. Therefore, the cracking strain associated with this segment reflects tension stiffening along with the occurrence of multiple cracking hardening. Following this segment, the third part of the curve in figure 1(c) signifies the transition into the softening phase, and the cracking strain in this region is utilized to characterize the softening phase with subsequent failure. The damping effect has not been considered since the

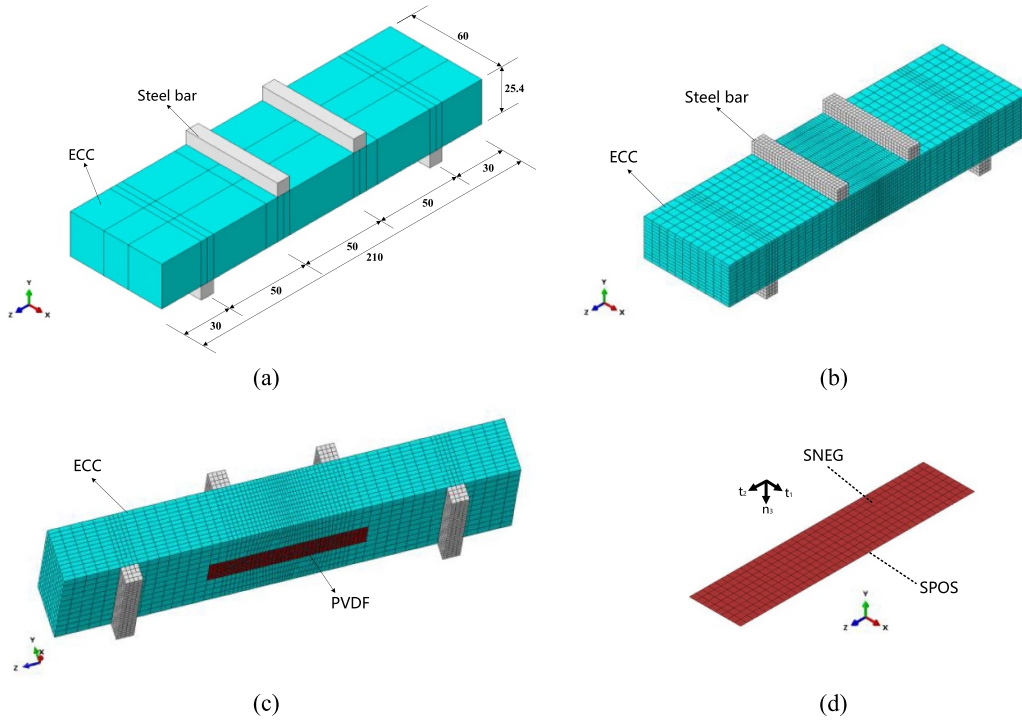


Figure 6. Mechanical model of bendable PVA-ECC with surface-mounted PVDF, (a) model configuration (unit: mm), (b) model meshing, (c) location of the PVDF film attached, (d) shell element for PVDF film.

Table 3. CDP model parameters for PVA-ECC.

ρ_{ECC} (kg m ⁻³)	E_0 (GPa)	ν_{ECC}	σ_{b0}/σ_{c0}	K_c	ψ	ε_{cc}	Viscosity parameter
1870	28	0.2	1.16	0.667	35	0.1	0.001

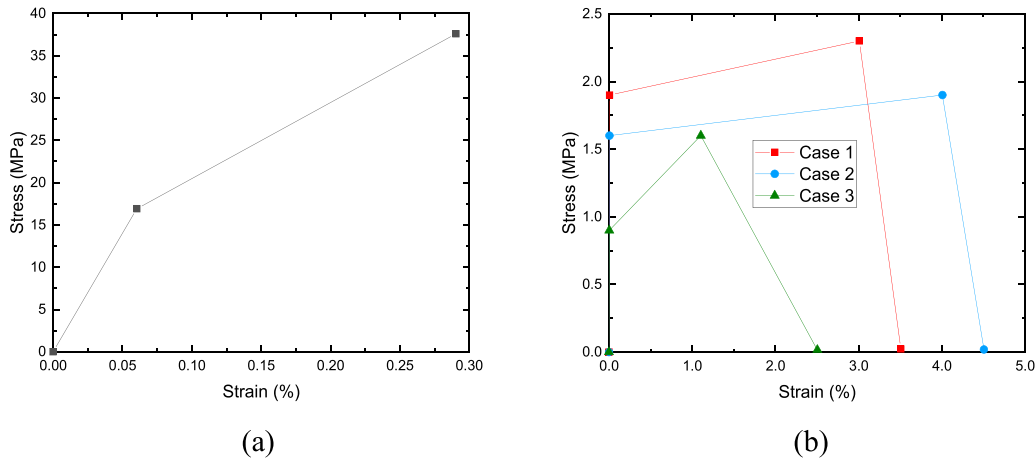


Figure 7. Stress-strain relationship of the ECC, (a) under uniaxial compression, (b) under uniaxial tension.

loading rates are low. Mesh size dependence analysis has been performed to determine the optimized mesh (see appendix A), which ensures the accuracy and reliability of the model while reducing computational cost. Due to complex links of constraints and interactions in the model, double-precision analysis for Abaqus/Explicit was adopted to ensure the desired accuracy of the solution.

3.3. Interaction between PVDF and ECC specimen

As displayed in figure 6(c), PVDF is surface-mounted on the bottom surface of the specimen at the mid-span. Generally, the thickness of a PVDF film is a range of 20–40 μm , which is much thinner than its length and width. If the PVDF film is modeled by solid elements with a very small size to consider

Table 4. Compressive behavior parameters.

Yield stress (MPa)	Inelastic strain (%)
16.92	0
37.6	0.23

Table 5. Tensile behavior parameters.

Case 1		Case 2		Case 3	
Yield stress (MPa)	Cracking strain (%)	Yield stress (MPa)	Cracking strain (%)	Yield stress (MPa)	Cracking strain (%)
1.9	0	1.6	0	0.9	0
2.3	3.0	1.9	4.0	1.6	1.1
0.023	3.5	0.019	4.5	0.016	2.5

its thickness, it enforces the entire simulation to run using a very small integration time increment, which inevitably results in very fine meshes and correspondingly prohibitive analysis time. Instead, the PVDF film can be assumed by using shell elements due to its tiny thickness and linear-elastic deformation. The use of shell elements for PVDF in this study can greatly reduce the computational cost while keeping the model fidelity (see figure 6(d)). The shell element in Abaqus adopted the local coordinate system with two tangential directions of t_1, t_2 (corresponding to positive x, z direction in the global coordinate system) and the normal direction of n_3 (corresponding to negative y direction in the global coordinate system). SNEG refers to the face of the PVDF film that is in contact with the ECC specimen. SPOS refers to the other side of the PVDF film that is not in contact with the ECC specimen. The strain in these two faces was included to calculate the average strain of the PVDF film since the shell element has several integration points along the thickness. Surface interaction was used between PVDF and the bottom surface of the ECC specimen. In Abaqus, hard contact is used to minimize the penetration of the slave surface into the master surface at the constraint locations. Herein, hard contact was adopted to minimize the overclosure of PVDF and the bottom surface of the ECC specimen. Moreover, no separation relationship was used to prevent the two surfaces from separating in the normal direction after contact. In the tangential direction, sliding friction with a friction coefficient was adopted for simulating the relative slip behavior of the ECC specimen and the PVDF film. The value of the tangential sliding friction coefficient was influenced by factors such as the contact materials (specifically, PVDF film and ECC), their bonding conditions and contact pressure under different loading rates. The tangential sliding friction coefficient in the energy harvesting model was determined by comparison with experiment results regarding the output voltage. In the simulation, the sliding friction coefficients between the PVDF film and the specimen under loading rates of 0.5 mm s^{-1} , 1.0 mm s^{-1} and 2.0 mm s^{-1} are 0.005, 0.0063, 0.065, respectively.

3.4. Piezoelectric model for the PVDF film

Figure 8(a) gives the configuration of a PVDF film with a length of l_p , a width of w_p and a height of h_p . The piezoelectric

film is bonded to the underside surface of the ECC specimen at pure moment segment. Thus, the small bending behavior of the piezoelectric film is mainly controlled by the axial strain in the length direction (the direction 1), especially when the deflection at the mid-point is not so much. The average axial strain of the PVDF film obtained from the mechanical model was imposed on one end of the film by an average axial displacement loading, which can be obtained by the product of the length and the axial strain of the film (equation (29)). The other end of the film is fixed

$$u_{\text{ave}}(t) = l_p \varepsilon_{\text{ave}}(t) \quad (29)$$

An eight-node linear piezoelectric brick element C3D8E in ABAQUS was adopted to simulate the piezoelectric effect of the PVDF film induced by the bending ECC. The element has both the mechanical degree of freedom (displacements) and electrical degree of freedom (electric potential), which can be calculated simultaneously. As shown in figure 8(b), the three-axis (i.e. the thickness direction) was set as the poling direction in the FE model for piezoelectric simulation. The bottom surface of the PVDF film was set as the ground electrode (i.e. zero potential). The top surface of the PVDF film was set as an equipotential surface, which indicates that all nodes in this surface have the same electric potential of V_{top} . Herein, constraint equations were used to ensure that all nodes in a surface have the same electric potential. An implicit dynamic analysis was utilized to calculate the real-time voltage output generated from the PVDF film due to the piezoelectric effects. In experiments in literature [25], the Voltage data logger (ADC-20) was used to record open circuit voltage. Correspondingly, the piezoelectric model was utilized for calculating the open circuit voltage.

In the piezoelectric FE model, the PVDF film has an area of $73 \text{ mm} \times 16 \text{ mm}$ ($l_p \times w_p$) with a thickness of $40 \mu\text{m}$ (h_p). Herein, only the thickness of $40 \mu\text{m}$ can generate an electrical potential. The PVDF film was assigned with typical piezoelectric and mechanical properties of PVDF obtained from the literature [14, 25, 42, 46], as outlined in table 6. Wherein ρ_e is the density of PVDF. g_{31}, g_{33} are the piezoelectric voltage constants of PVDF. f_{eu} is the yield strength of PVDF. k_{31} is the electromechanical coupling factor of PVDF. P_e is the pyroelectric coefficient. ν_p is the Poisson's ratio. For small strains,

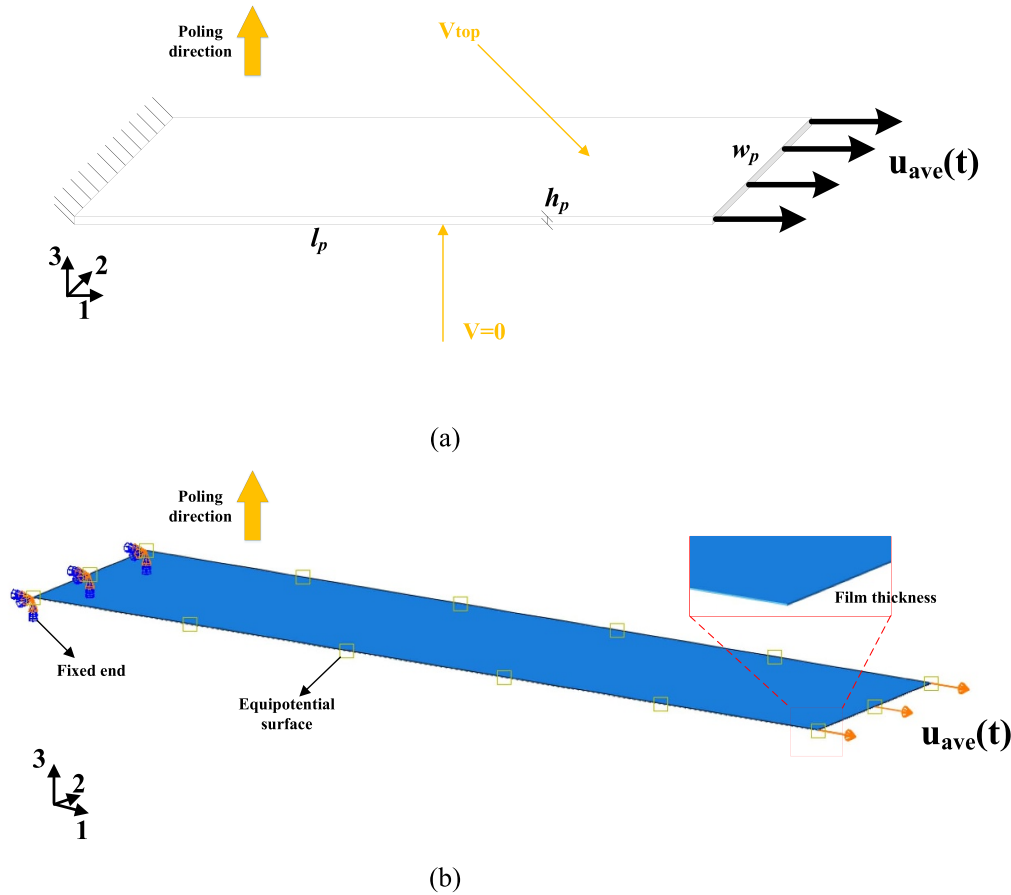


Figure 8. Piezoelectric model for the PVDF film, (a) the PVDF film applied by the average axial displacement, (b) FEM model based on piezoelectric elements.

Table 6. Piezoelectric and mechanical properties of PVDF.

Material properties			Material properties		
Value	Units		Value	Units	
ρ_e	1780	kg m^{-3}	E_e	2	GPa
ν_p	0.34	—	f_{eu}	45–55	MPa
d_{31}	23	pC/N	d_{32}	1.476	pC/N
d_{33}	−33.8	pC/N	d_{15}	20	pC/N
e_{33}	1.15×10^{-10}	F m^{-1}	g_{31}	216×10^{-3}	m^2/C
g_{33}	-330×10^{-3}	m^2/C	k_{31}	12%	—
P_e	30	$\text{C}/\text{m}^2 \cdot \text{K}$			

however, the material of the PVDF film is considered mechanically isotropic [29]. In appendix B, further verification of the piezoelectric model was done by using experimental data in literature [47].

3.5. Results and discussion

As shown in figure 9, the simulated results from the simplified method are in good agreement with experimental data [25]. The flexural stress–displacement curve refers to the left y-axis, and the output voltage–displacement curve refers to the right

y-axis. Herein, the midpoint displacement of the bottom surface of the specimen was considered. It is found that, under different loading rates, the flexural stress increases quickly with the increase of the midpoint displacement in the initial stage. Correspondingly, the output voltage also shows a rapid increase with the increase of the displacement during the initial stage. This is because that the specimen is initially located in the elastic and rapid strain-hardening range, which provides a rapid strain increment to generate a higher voltage increment. Then, when it enters the later plastic stage with a slow strain-hardening, the stress shows a relatively slow increase with the displacement increase. Accordingly, the output voltage slowly increases with the displacement increase during the later plastic stage.

As seen in figure 9, it is found that the output voltage increases as the loading rate increases. The simulated and experimental results for average output voltages at loading rates of 0.5 mm s^{-1} , 1.0 mm s^{-1} , and 2.0 mm s^{-1} are close. The simulated values are around 5.69 mV, 8.05 mV, and 19.58 mV, respectively, while the experimental values are 6.01 mV, 10.59 mV, and 21.24 mV. This agreement between the simulated voltage and experimental data indicates that the developed model is able to calculate the effects of dynamic loading rates on the flexural stress and corresponding output voltage.

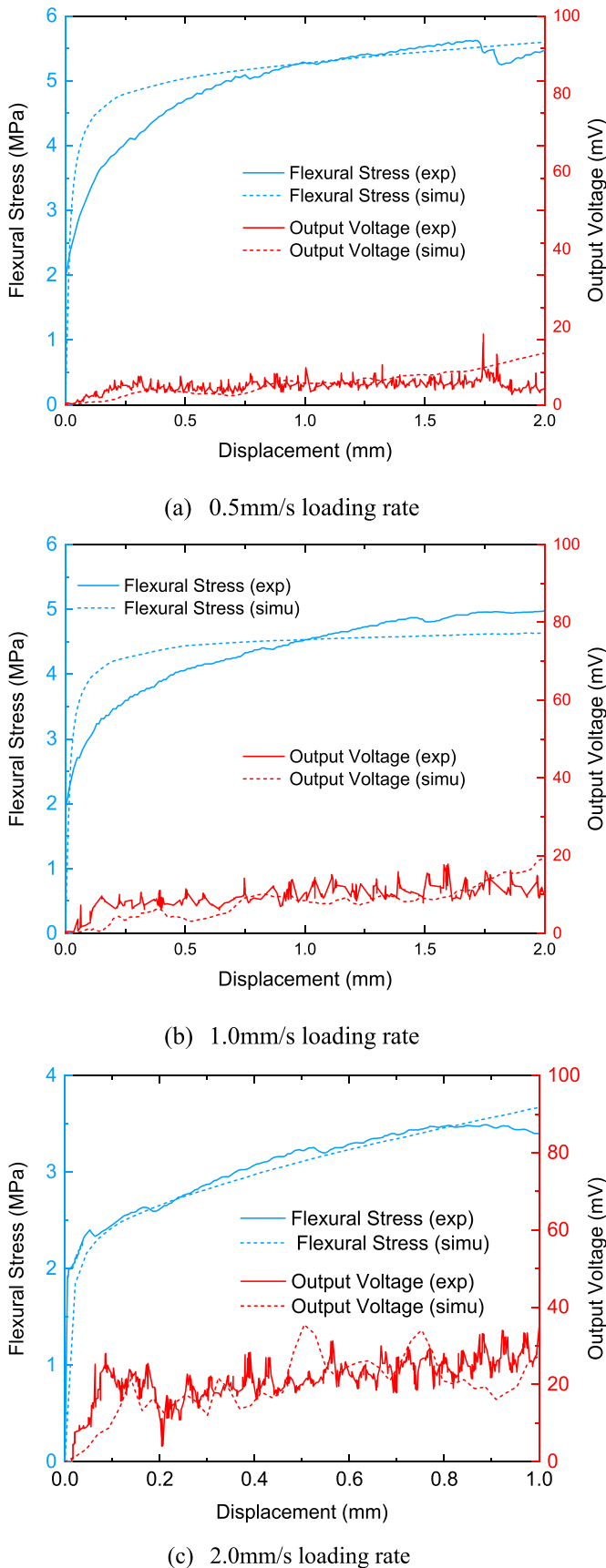


Figure 9. Comparisons of the flexural stress and output voltage versus mid-point displacement between experimental data [25] and simulated results under different loading rates.

Figure 10 gives the strain distribution of the ECC specimen and the PVDF film under different loading rates of 0.5 mm s^{-1} , 1.0 mm s^{-1} , 2.0 mm s^{-1} , when the corresponding mid-point displacements reach 2.0 mm, 2.0 mm, 1.0 mm, respectively. PE33 for the ECC specimen is the z -direction plain strain in the global coordinate system. LE22 for the PVDF film is the t_2 -direction tangential strain in the local coordinate system of the shell element (parallel to the z -axis in the global coordinate system). It can be found that the ECC specimen exhibits a strong strain-hardening behavior, and the strain of the PVDF film is much lower than that of the ECC due to the sliding friction between the two.

As indicated in equation (28), the output voltage generated by the PVDF film is linearly associated with the axial strain applied on the film. According to the manufacturer, more than 10 mV can be generated by the PVDF per micro strain [25]. In the model, the axial strain of the PVDF film is extracted under different loading rates, as shown in figure 11. Wherein the displacement also indicates the mid-point displacement as in figure 9 for different loading rates. ε_{ave} refers to the axial average strain of the PVDF film. It can be found that the axial average strain of the PVDF film exhibits a comparable relationship to the output voltage concerning mid-point displacement. Similar to the output voltage, the axial strain of the film was higher under 2.0 mm s^{-1} loading rate, and decreases with the decrease of the loading rate. The axial strain of the film under 1.0 mm s^{-1} loading rate is relatively close to that under 0.5 mm s^{-1} loading rate since the low loading rates of 0.5 mm s^{-1} and 1.0 mm s^{-1} are close to quasi-static loading. As indicated in this model, the axial strain of the film is significantly influenced by the sliding friction coefficient between the film and the specimen. Accordingly, the sliding friction coefficient under 1.0 mm s^{-1} loading rate is 0.0063, which is slightly larger than 0.005 under 0.5 mm s^{-1} loading rate. The sliding friction coefficient under 2.0 mm s^{-1} loading rate is 0.065, which is ten times higher than that under 1.0 mm s^{-1} loading rate or 0.05 mm s^{-1} loading rate. This friction-induced voltage mechanism in this model reveals that a higher loading rate causes more frictional contact between the PVDF film and the ECC specimen, which results in a higher axial strain of the film to generate more output voltage.

In the experiment, the fluctuations for the voltage measurement are mainly from environmental influences (e.g. external current frequency of the data recorder). The CDP model considers the ECC specimen as a homogeneous solid, which cannot reflect the heterogeneity of the specimen. This leads to some differences in the flexural stress-midpoint displacement curves between the simulation and experiment. The voltage differences between the simulated results and measured data may arise from these factors: The simulated flexural stress-midpoint displacement curve is not completely matched with the experimental one; the soldering point on the PVDF film has not been considered in the model; due to deterioration, the piezoelectric coefficient could decrease up to 5% according to the literature [48]; There may be some difference between the actual piezoelectric properties and the values provided

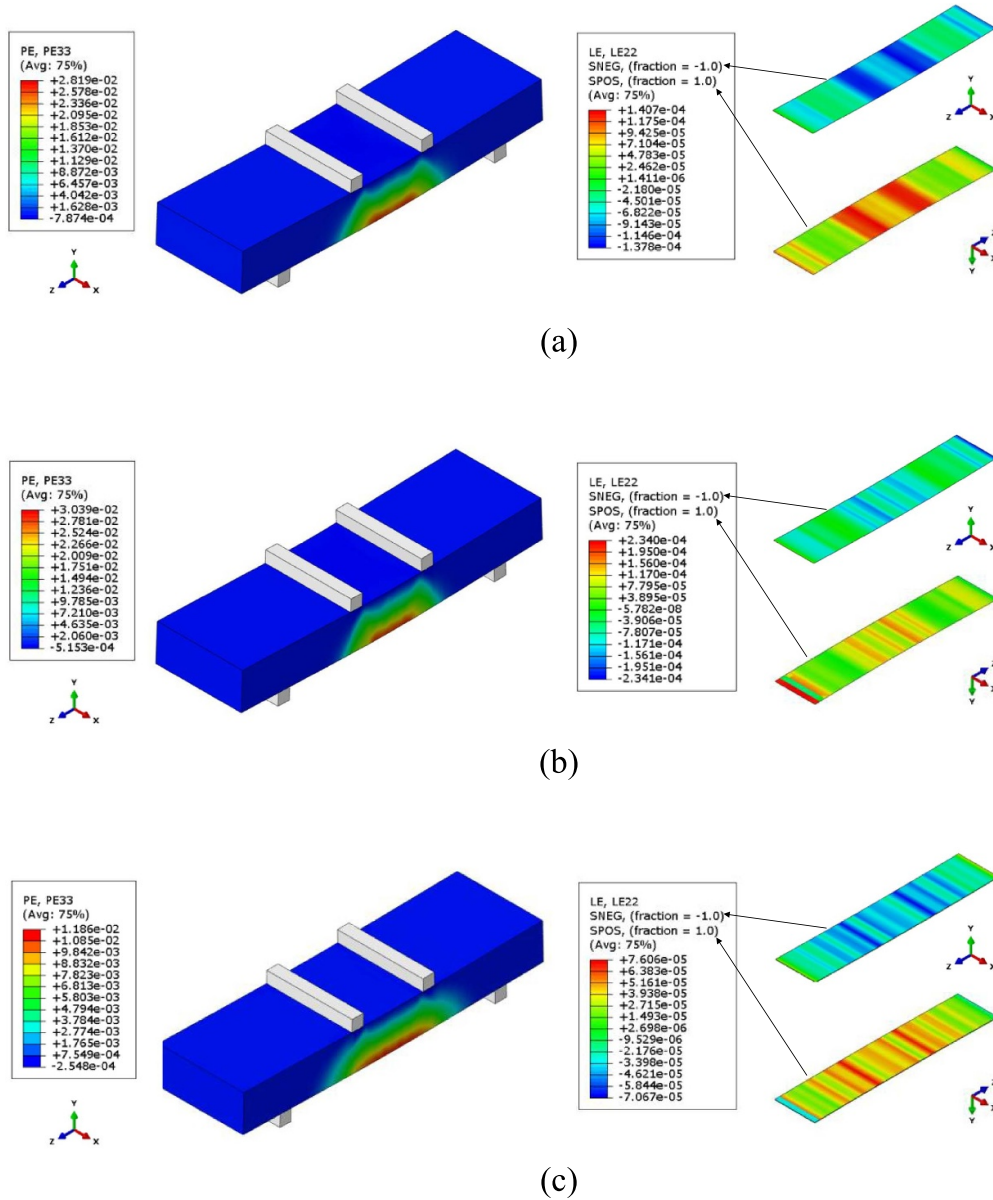


Figure 10. Strain distribution of the PVA-ECC specimen and PVDF film under 0.5 mm/s loading rate (a), 1.0 mm s⁻¹ loading rate (b), and 2.0 mm s⁻¹ loading rate (c).

by the manufacturer; the internal impedance of the electrical measurement instrument has an electrical loading effect and reduction of output open circuit voltage.

In the FEM-based piezoelectric model, the axial strain of the film is applied to the film as the time-history loading. In the FEM, the dielectric constants and the mechanical properties of the PVDF film are considered to be isotropic. Damping was not considered since loading rates were low. Dielectric loss was not considered due to the very short loading time and constant loading rates without frequency [49]. Compared to the simplified method, the FEM considers the inertia force due to mass, and d_{32} , d_{33} during the dynamic analysis. Figure 12 gives a comparison of the simulated voltage results between FEM and simplified method under different loading rates.

As shown in figure 12, there is a good agreement between the FEM and simplified method. Nonetheless, there remains a very small difference between the two results when the loading rate increases from 0.5 mm s⁻¹ to 2.0 mm s⁻¹. This is because the FEM takes into account the mass of the PVDF film to consider inertial force, and the kinetic energy also increases with the increase of loading rate, both of which are not considered by the simplified method. The small difference reveals that the PVDF film mass is very small, which has a minor influence on its output voltage in the FEM. The output voltage is mainly from the strain energy of the film during its mechanical deformation. Although damping effects on the piezoelectric simulation are not considered since loading rates were low, the FE model is able to consider it, while the

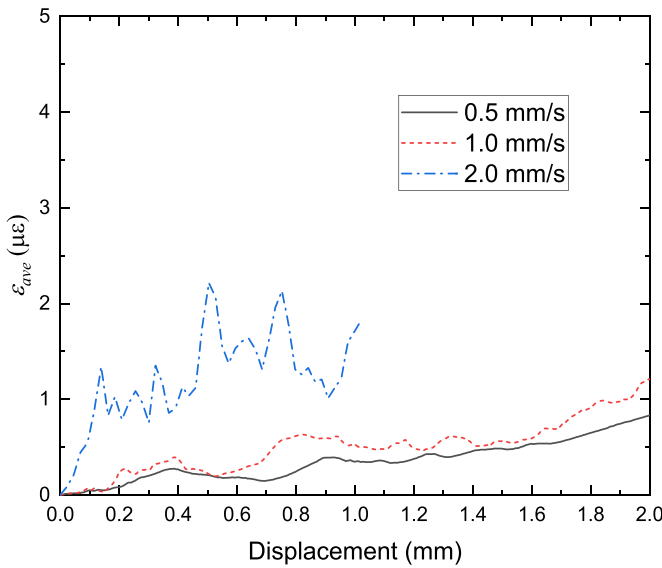


Figure 11. Comparisons of the axial average strain versus mid-point displacement under different loading rates.

simplified method is not. Figure 13 also gives voltage distributions of the PVDF film in FEM under different loading rates of 0.5 mm s^{-1} , 1.0 mm s^{-1} , 2.0 mm s^{-1} , when the corresponding mid-point displacements reach 2.0 mm, 2.0 mm, 1.0 mm, respectively. The unit in the legend of figure 13 is volt. As the ground electrode, the electric potential on the bottom surface was 0 volt. It can be found that the voltages distribute along the film thickness direction with an electric field strength. The electric potential on the top surface increases as the loading rate increases. They are 13.20 mV, 19.10 mV, 28.77 mV under different loading rates of 0.5 mm s^{-1} , 1.0 mm s^{-1} , 2.0 mm s^{-1} , respectively, when corresponding ECC specimens reach near their peak stresses.

4. Parametric studies

As indicated in equations (11)–(28), the compliance tensor s^E , the piezoelectric strain tensor d , the dielectric permittivity tensor ϵ^T , and the PVDF film thickness t_p are important parameters for calculating the output voltage. Hence, this section focuses on parametric studies to examine the effects of PVDF film thickness, elastic modulus of PVDF film, piezoelectric constants and dielectric constants of PVDF film on the output voltage by a combination of mechanical and electrical models. The following parametric analyses were based on the validated model under 2.0 mm s^{-1} loading rate presented in section 3.

4.1. PVDF film thickness

As mentioned before, the PVDF film is generally laminated to a polyester substrate of a certain thickness as a protective layer. In the mechanical model, the PVDF film is considered with its total thickness including the protective layer. In the electrical model, the PVDF film is only modeled with its thickness to generate voltage. In practical applications, the total

thickness of PVDF films is different, and its effects on the mechanical and electrical results need to be studied. Herein, three PVDF films with a total thickness of 0.1 mm, 0.165 mm, 0.2 mm were chosen based on the literature [20, 21, 50]. All PVDF films have the same thickness of $40 \mu\text{m}$. As displayed in figure 14, the PVDF film thickness has no effect on the flexural stress-mid-point displacement curve in the mechanical model. However, it has a great influence on the output voltage in the electrical model. In general, the output voltage increases as the increase of the PVDF film thickness. The average output voltages for the PVDF film thickness of 0.1 mm, 0.165 mm, 0.2 mm are 11.28 mV, 17.43 mV, 26.21 mV, respectively.

4.2. Elastic modulus of PVDF film

Generally, the elastic modulus of PVDF films is 2–4 GPa according to the literature [25, 47, 51]. In the mechanical model, the mechanical behavior of PVDF film mainly depends its elastic modulus; in electrical model, its elastic modulus has a profound effect on the generated voltage due to piezoelectric effect. The effects of elastic modulus of PVDF films on the mechanical and electrical results were quantified in this section, wherein PVDF films with 2 GPa, 3 GPa, 4 GPa were chosen for the parametric analysis. As shown in figure 15, the PVDF elastic modulus has a negligible effect on the flexural stress-mid-point displacement curve in the mechanical model. Nevertheless, it presents a certain effect on the output voltage wherein the PVDF film with a larger elastic modulus generates relatively more output voltage. The average output voltages for PVDF films with 2 GPa, 3 GPa, 4 GPa are 19.58 mV, 20.46 mV, 21.39 mV, respectively.

4.3. Piezoelectric constants

In piezoelectric effect, piezoelectric constants present the magnitude of electromechanical coupling, which determines the conversion degree of strain energy to electrical energy. The inverse piezoelectric effect of PVDF is very small, and its influence on the mechanical model is not considered. As indicated in equation (25), d_{31} is of great importance for the output voltage, and was chosen for parametric study with three values of 13.58 pC/N, 18 pC/N, 23 pC/N based on literatures [14, 25, 46]. As indicated in figure 16, a higher piezoelectric constant of the PVDF film results in more output voltage, but the piezoelectric constant will not change the trend of output voltage-displacement curve.

4.4. Dielectric constants

As indicated in equation (27), the dielectric constant ϵ_{33} is used to calculate the electric capacity of the PVDF film, and thus has a great influence on the output voltage. In general, the dielectric constant ϵ_{33} of the PVDF film takes a value from $1.06 \times 10^{-10} \text{ F m}^{-1}$ to $1.15 \times 10^{-10} \text{ F m}^{-1}$, which corresponds to a relative dielectric constant of 12 F m^{-1} to 13 F m^{-1} [25]. Similarly, the inverse piezoelectric effect due

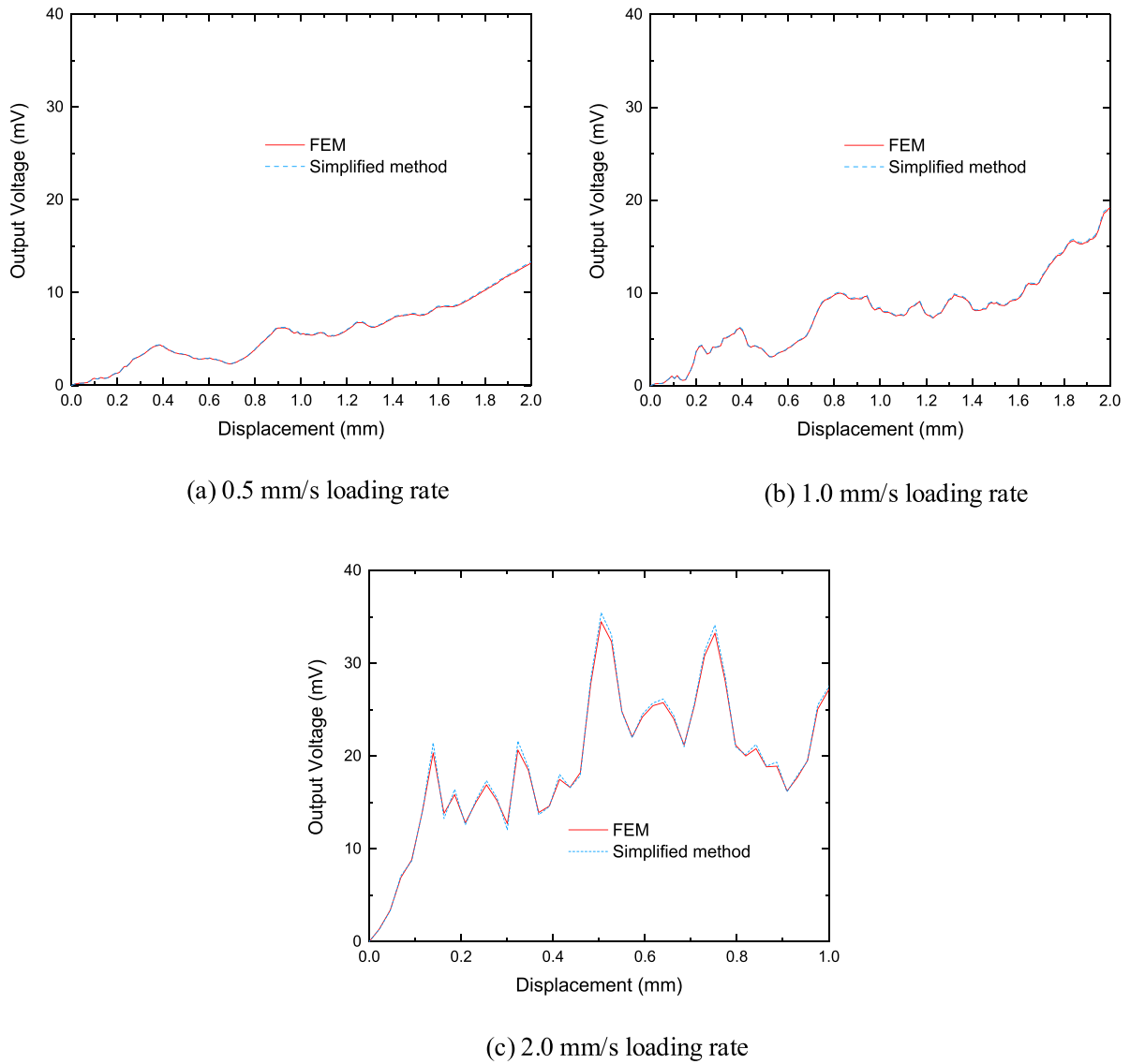


Figure 12. Comparisons of the output voltage versus mid-point displacement between FEM and simplified method under different loading rates.

to the dielectric constant is very small in terms of PVDF, and has no effect on the mechanical model. Herein, three dielectric constants of 1.06×10^{-10} , 1.11×10^{-10} , 1.15×10^{-10} (corresponding to relative dielectric constants of 12, 12.5, 13) were chosen for a parametric analysis regarding their effects on the output voltage in the electrical model. As indicated in figure 17, as the dielectric constant of the PVDF film increases, there is a slight decrease in the output voltage. Still, the dielectric constant has no effect on the trend of output voltage-displacement curve.

5. Conclusions

In this work, an energy harvesting model has been developed for calculating the output voltage of ECC specimen incorporating flexible PVDF. Several important conclusions can be drawn as follows

- (1) In the mechanical model, the dynamic flexural behavior of ECC was simulated by the CDP model. The surface-mounted PVDF film was simplified as a shell element to reduce computation cost while keep calculation accuracy. The force transfer between ECC and PVDF due to the bond layer was simulated by a sliding friction model. The good agreement between simulation results and experimental data in literature proves the accuracy and reliability of the proposed model.
- (2) In the piezoelectric simulation, both FEM and simplified formulas were used to calculate the output voltage from the PVDF film, and the two results correspond to each other. Compared to simplified formulas, FEM can be used in complex stress states with consideration of mass, damping, and material heterogeneity for mechanical and piezoelectric parameters.
- (3) In the PVDF-ECC energy harvesting system, the output voltage generated increases with the increase of the

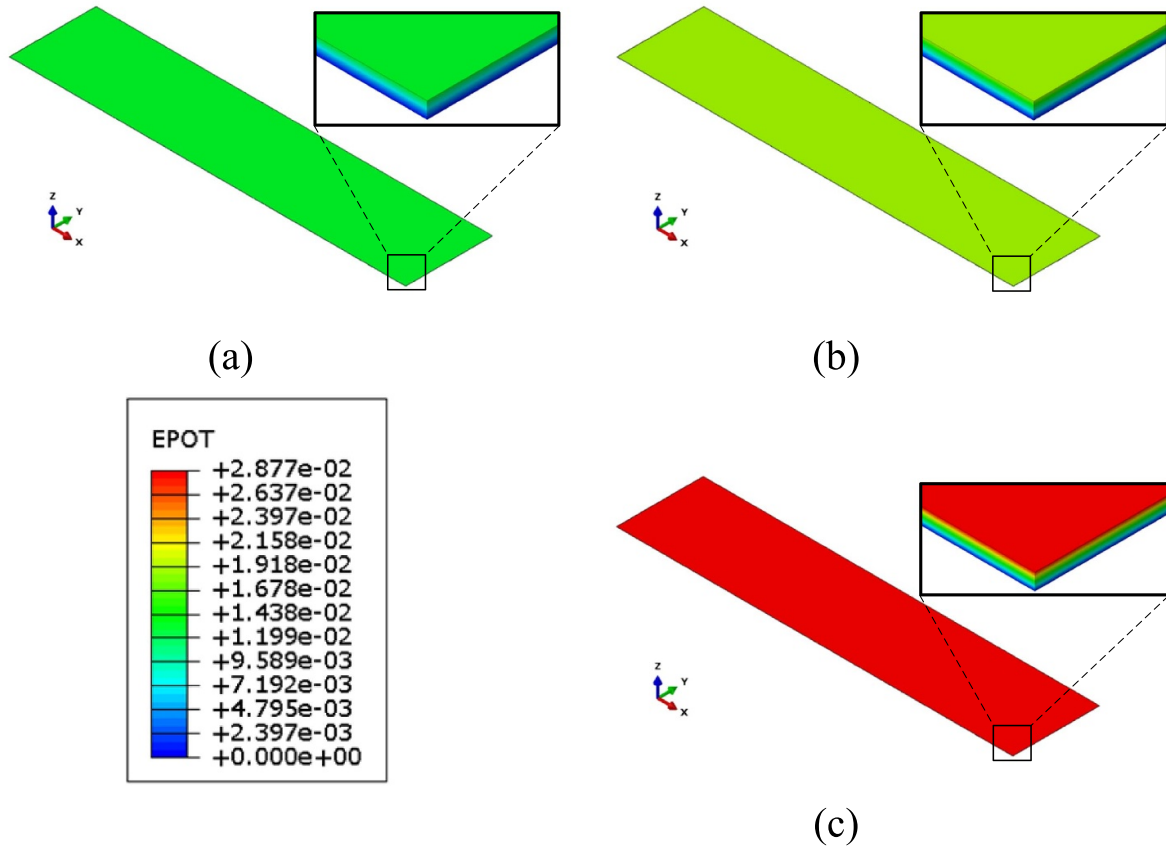


Figure 13. Voltage distribution of the PVDF film under 0.5 mm s^{-1} loading rate (a), 1.0 mm s^{-1} loading rate (b), and 2.0 mm s^{-1} loading rate (c).

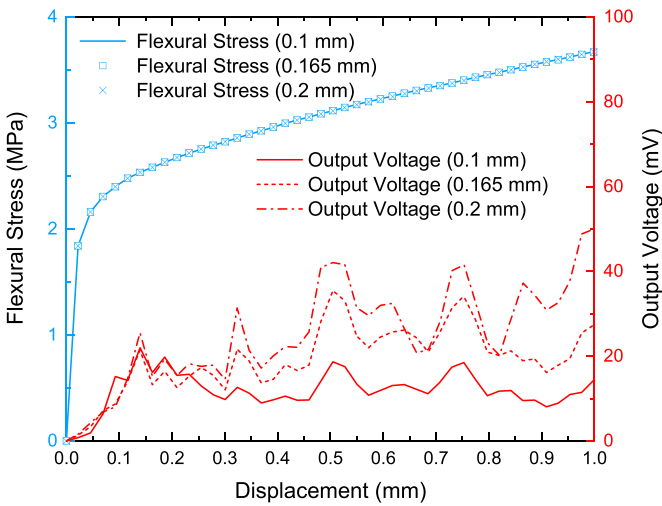


Figure 14. Flexural stress and output voltage versus mid-point displacement for different thicknesses.

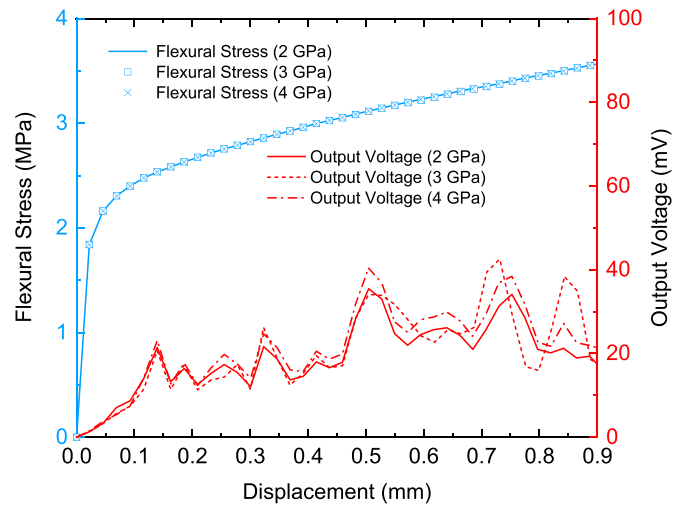


Figure 15. Flexural stress and output voltage versus mid-point displacement for different elastic modulus.

dynamic loading rate. This is because a greater dynamic loading rate enhances the interaction between the PVDF and the ECC specimen, which results in a higher friction coefficient between the two. Thus, a higher axial strain is transferred to the PVDF film to generate a higher output voltage.

(4) The parametric analysis results show that the output voltage increases as the increase of the PVDF film thickness. The PVDF film with a higher elastic modulus generates relatively more output voltage. A higher piezoelectric constant of the PVDF film results in more output voltage. As the dielectric constant of the PVDF film decreases,

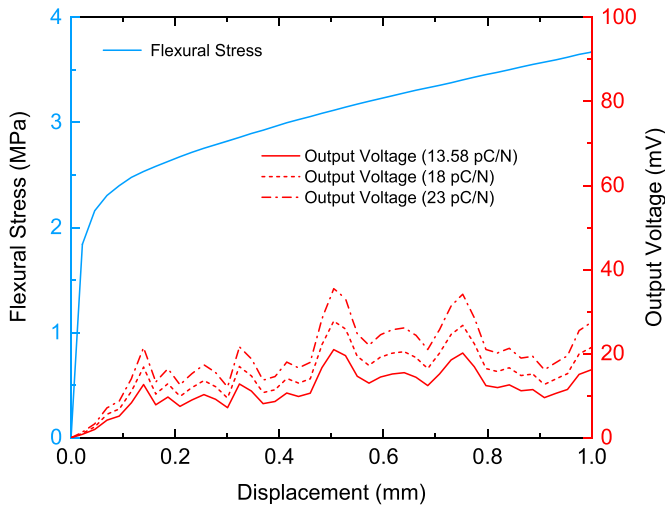


Figure 16. Flexural stress and output voltage versus mid-point displacement for different piezoelectric constants.

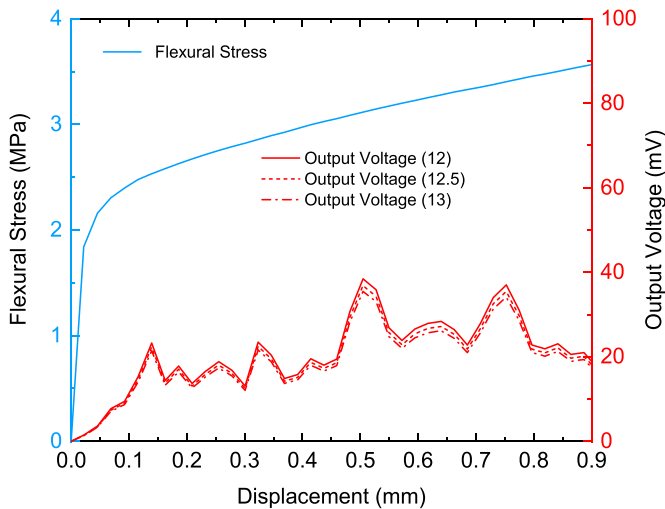


Figure 17. Flexural stress and output voltage versus mid-point displacement for different dielectric constants.

there is a slight increase in the output voltage. However, these four parameters have no effect on the mechanical model. In future research, an optimal analysis needs to be conducted on the output voltage of the PVDF-ECC energy harvesting system, taking into account these parameters.

- (5) This newly proposed model considers a series of energy harvesting parameters, including dynamic loading rates, PVA-ECC mechanical properties, interaction between PVA-ECC and PVDF, geometry and material properties of PVDF. The theoretical model developed in this study can be of great use in the design and optimization for harvesting energy from engineering cementitious materials incorporating flexible piezoelectric films.

This study introduced an energy harvesting model designed for the PVDF film, which is surface-mounted on the underside of the ECC beam at the mid-span during a flexural test. The segment of the PVDF film bonded in the pure bending region

leverages the film's flexural capability to produce voltage. In practical applications, the model is applicable for situations where the PVDF film is surface-mounted in structural locations primarily subjected to flexural stress. Energy harvesting experiments in the literature [25] are often brief, lasting only seconds per sample, allowing assumptions about constant temperature, humidity, and aging. However, the current model does not account for their potential influence on the voltage output of the PVDF film. In prolonged use for energy harvesting, investigations should explore variables like temperature, humidity, and aging to thoroughly grasp their impact on the voltage output of the PVDF film in future studies. Specifically, it is important to consider the pyroelectric effect of the PVDF film due to its sensitivity to ambient temperature changes.

Data availability statement

All data that support the findings of this study are included within the article (and any supplementary files).

Acknowledgments

Jinbao Xie and Zhi Wan would like to acknowledge the funding supported by China Scholarship Council (CSC) under the grant CSC No. 202006260045, 201906220205. Yading Xu and Branko Šavija acknowledge the financial support of the European Research Council (ERC) within the framework of the ERC Starting Grant Project 'Auxetic Cementitious Composites by 3D printing (ACC-3D)', Grant Agreement Number 101041342. Views and opinions expressed are however those of the author(s) only and do not necessarily reflect those of the European Union or the European Research Council. Neither the European Union nor the granting authority can be held responsible for them.

Conflict of interests

The authors declare that they have no known competing financial interests or personal relationships that could have appeared to influence the work reported in this paper.

Appendix A. Mesh dependence analysis

An analysis of mesh dependence was conducted to identify the optimal mesh, as depicted in figure A1(a). The same model with a refined mesh was established in figure A1(b). Figure A1(c) presents a comparison of the flexural stress-midpoint displacement curves between the two mesh configurations under 2.0 mm s^{-1} loading rates. It is observed that the simulated results obtained with the current mesh remain in agreement with those obtained using a refined mesh, demonstrating the robustness, reliability, and accuracy of the model.

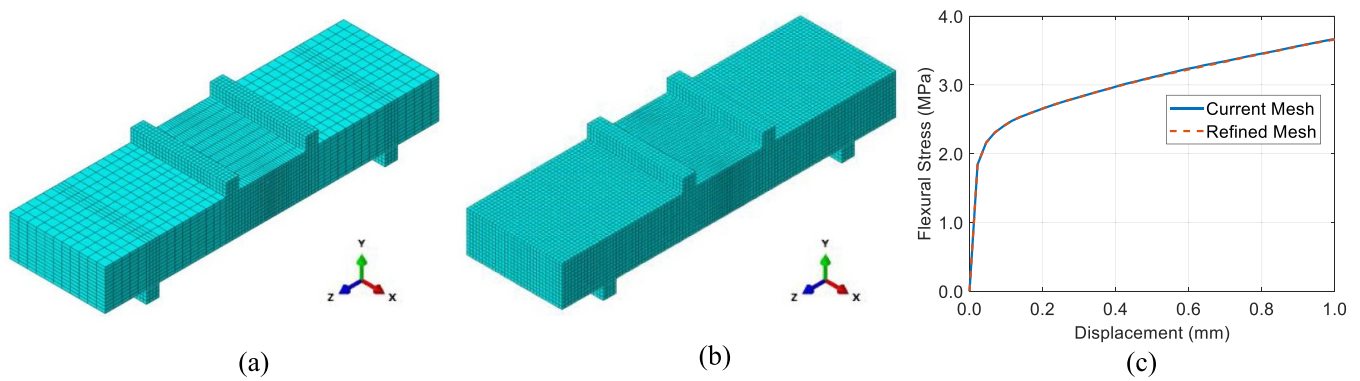


Figure A1. Mesh dependence analysis, (a) current mesh, (b) refined mesh, (c) comparison of the results of the two mesh cases.

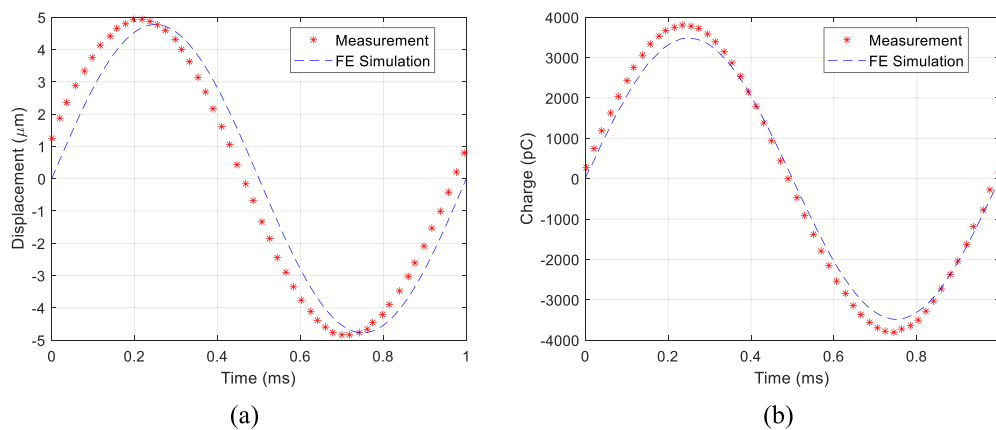


Figure B1. FE model validation of the mechanical behavior (a) and piezoelectric behavior (b) for PVDF film.

Appendix B. Verification of the piezoelectric model

Another experimental data in literature [47] was used to validate the FEM-based piezoelectric model. In their experiments setup [47], two PMMA clamps were used to hold a piezo film sensor subjected to stretching forces applied by a smart shaker (TMS K2007E1). To simultaneously measure force and acceleration, a force sensor (Kistler 9301B) was mounted on one holder, while an accelerometer (Kistler 8714B100M5) was placed on the other holder. Additionally, the piezo film (Measurement Specialties DT1-52kK/L w/rivets) was connected to a charge amplifier (Kistler 5165A4K) and measured as well. The smart shaker signal was subjected to AD conversion and signal driving using National Instrument hardware (cDAQ9178, 9234, 9239, 9263), controlled by a PC through MATLAB. The PVDF film is sized at 41 mm × 16 mm × 0.9 mm. The PVDF film was characterized with conventional piezoelectric and mechanical properties sourced from literature [14, 25, 42, 46], as detailed in table 6. The piezoelectric model applied to the PVDF film in section 3.4 was similarly utilized for this validation, employing identical element type, boundary conditions, and solving techniques. One end of the PVDF film was applied by a displacement loading with a sine wave at 1 kHz. Figure B1 presents a comparison between the simulated results and

measurements reported in the literature [47], providing additional validation for the piezoelectric model employed in this study.

ORCID iDs

Jinbao Xie  <https://orcid.org/0000-0002-0357-2333>

Yading Xu  <https://orcid.org/0000-0001-5825-4175>

References

- [1] Fan T, Zou G and Yang L 2015 Nano piezoelectric/piezomagnetic energy harvester with surface effect based on thickness shear mode *Composites B* **74** 166–70
- [2] Yaqoob U, Uddin A S M I and Chung G-S 2018 Synthesis of poly(vinylidene fluoride-trifluoroethylene)-0.65Pb(Mg_{1/3}Nb_{2/3})O₃-0.35PbTiO₃-reduced graphene oxide-composite sheet and its application to flexible energy harvesting *Composites B* **136** 92–100
- [3] Zhu G, Lin Z-H, Jing Q, Bai P, Pan C, Yang Y, Zhou Y and Wang Z L 2013 Toward large-scale energy harvesting by a nanoparticle-enhanced triboelectric nanogenerator *Nano Lett.* **13** 847–53
- [4] Ghafari E, Severgnini F, Ghahari S, Feng Y, Lee E J, Zhang C, Jiang X and Lu N 2018 Thermoelectric nanocomposite for energy harvesting *Multifunctional Nanocomposites for*

- Energy and Environmental Applications* (Wiley) pp 173–202
- [5] Beeby S P, Torah R N, Tudor M J, Glynne-Jones P, O'Donnell T, Saha C R and Roy S 2007 A micro electromagnetic generator for vibration energy harvesting *J. Micromech. Microeng.* **17** 1257–65
 - [6] Lu N and Ferguson I 2013 III-nitrides for energy production: photovoltaic and thermoelectric applications *Semicond. Sci. Technol.* **28** 074023
 - [7] Zi Y, Lin L, Wang J, Wang S, Chen J, Fan X, Yang P-K, Yi F and Wang Z L 2015 Triboelectric–pyroelectric–piezoelectric hybrid cell for high-efficiency energy-harvesting and self-powered sensing *Adv. Mater.* **27** 2340–7
 - [8] Xiong H and Wang L 2016 Piezoelectric energy harvester for public roadway: on-site installation and evaluation *Appl. Energy* **174** 101–7
 - [9] Zhao H, Yu J and Ling J 2010 Finite element analysis of Cymbal piezoelectric transducers for harvesting energy from asphalt pavement *J. Ceram. Soc. Jpn.* **118** 909–15
 - [10] Wang C, Wang S, Gao Z and Wang X 2019 Applicability evaluation of embedded piezoelectric energy harvester applied in pavement structures *Appl. Energy* **251** 113383
 - [11] Huang K, Zhang H, Jiang J, Zhang Y, Zhou Y, Sun L and Zhang Y 2022 The optimal design of a piezoelectric energy harvester for smart pavements *Int. J. Mech. Sci.* **232** 107609
 - [12] Cao Y, Li J, Sha A, Liu Z, Zhang F and Li X 2022 A power-intensive piezoelectric energy harvester with efficient load utilization for road energy collection: design, testing, and application *J. Clean. Prod.* **369** 133287
 - [13] Jung I, Shin Y-H, Kim S, Choi J-Y and Kang C-Y 2017 Flexible piezoelectric polymer-based energy harvesting system for roadway applications *Appl. Energy* **197** 222–9
 - [14] Roy Chowdhury A, Saurabh N, Kiran R and Patel S 2021 Effect of porous auxetic structures on low-frequency piezoelectric energy harvesting systems: a finite element study *Appl. Phys. A* **128** 62
 - [15] Wang L, Zhao L, Jiang Z, Luo G, Yang P, Han X, Li X and Maeda R 2019 High accuracy comsol simulation method of bimorph cantilever for piezoelectric vibration energy harvesting *AIP Adv.* **9** 095067
 - [16] Kashfi M, Fakhri P, Amini B, Yavari N, Rashidi B, Kong L and Bagherzadeh R 2020 A novel approach to determining piezoelectric properties of nanogenerators based on PVDF nanofibers using iterative finite element simulation for walking energy harvesting *J. Ind. Text.* **51** 531S–53S
 - [17] Mateu L and Moll F 2005 Optimum piezoelectric bending beam structures for energy harvesting using shoe inserts *J. Intell. Mater. Syst. Struct.* **16** 835–45
 - [18] Mateu L and Moll F 2006 Appropriate charge control of the storage capacitor in a piezoelectric energy harvesting device for discontinuous load operation *Sens Actuators A* **132** 302–10
 - [19] Moro L and Benasciutti D 2010 Harvested power and sensitivity analysis of vibrating shoe-mounted piezoelectric cantilevers *Smart Mater. Struct.* **19** 115011
 - [20] Wang Y, Zhu X, Zhang T, Bano S, Pan H, Qi L, Zhang Z and Yuan Y 2018 A renewable low-frequency acoustic energy harvesting noise barrier for high-speed railways using a Helmholtz resonator and a PVDF film *Appl. Energy* **230** 52–61
 - [21] Vatansver D, Hadimani R L, Shah T and Siores E 2011 An investigation of energy harvesting from renewable sources with PVDF and PZT *Smart Mater. Struct.* **20** 055019
 - [22] Xu Y, Zhang H, Schlangen E, Luković M and Šavija B 2020 Cementitious cellular composites with auxetic behavior *Cem. Concr. Compos.* **111** 103624
 - [23] Cahill P, Nuallain Nora Aine N, Jackson N, Mathewson A, Karoumi R and Pakrashi V 2014 Energy harvesting from train-induced response in bridges *J. Bridge Eng.* **19** 04014034
 - [24] Xu Y, Schlangen E, Luković M and Šavija B 2021 Tunable mechanical behavior of auxetic cementitious cellular composites (CCCs): experiments and simulations *Constr. Build. Mater.* **266** 121388
 - [25] Su Y-F, Kotian R R and Lu N 2018 Energy harvesting potential of bendable concrete using polymer based piezoelectric generator *Composites B* **153** 124–9
 - [26] Pan H H and Guan J-C 2022 Stress and strain behavior monitoring of concrete through electromechanical impedance using piezoelectric cement sensor and PZT sensor *Constr. Build. Mater.* **324** 126685
 - [27] IEEE Standards Board 1988 IEEE standard on piezoelectricity ANSI/IEEE standard 176–1987 (Institute of Electrical and Electronics Engineers Inc)
 - [28] Lerch R 1990 Simulation of piezoelectric devices by two- and three-dimensional finite elements *IEEE Trans. Ultrason. Ferroelectr. Freq. Control* **37** 233–47
 - [29] Sirohi J and Chopra I 2000 Fundamental understanding of piezoelectric strain sensors *J. Intell. Mater. Syst. Struct.* **11** 246–57
 - [30] Faria R, Oliver J and Cervera M 1998 A strain-based plastic viscous-damage model for massive concrete structures *Int. J. Solids Struct.* **35** 1533–58
 - [31] Wu J Y, Li J and Faria R 2006 An energy release rate-based plastic-damage model for concrete *Int. J. Solids Struct.* **43** 583–612
 - [32] Feng D-C, Ren X-D and Li J 2018 Softened damage-plasticity model for analysis of cracked reinforced concrete structures *J. Struct. Eng.* **144** 04018044
 - [33] Zhou J, Pan J and Leung C K Y 2015 Mechanical behavior of fiber-reinforced engineered cementitious composites in uniaxial compression *J. Mater. Civil Eng.* **27** 04014111
 - [34] Meng D, Huang T, Zhang Y X and Lee C K 2017 Mechanical behaviour of a polyvinyl alcohol fibre reinforced engineered cementitious composite (PVA-ECC) using local ingredients *Constr. Build. Mater.* **141** 259–70
 - [35] Jothi Saravanan T and Singh Chauhan S 2022 Study on pre-damage diagnosis and analysis of adhesively bonded smart PZT sensors using EMI technique *Measurement* **188** 110411
 - [36] Nguyen B-P, Tran Q H, Nguyen T-T, Pradhan A M S, Huynh T-C and Lo Iudice F 2021 Understanding impedance response characteristics of a piezoelectric-based smart interface subjected to functional degradations *Complexity* **2021** 5728679
 - [37] Yan W and Chen W Q 2010 Structural health monitoring using high-frequency electromechanical impedance signatures *Adv. Civil Eng.* **2010** 429148
 - [38] Bhalla S and Soh C K 2004 Electromechanical impedance modeling for adhesively bonded piezo-transducers *J. Intell. Mater. Syst. Struct.* **15** 955–72
 - [39] Lim Y Y, Kwong K Z, Liew W Y H, Padilla R V and Soh C K 2018 Parametric study and modeling of PZT based wave propagation technique related to practical issues in monitoring of concrete curing *Constr. Build. Mater.* **176** 519–30
 - [40] Jung H J, Jabbar H, Song Y and Sung T H 2016 Hybrid-type (d33 and d31) impact-based piezoelectric hydroelectric energy harvester for watt-level electrical devices *Sens Actuators A* **245** 40–48
 - [41] Anton S R and Sodano H A 2007 A review of power harvesting using piezoelectric materials (2003–2006) *Smart Mater. Struct.* **16** R1–R21
 - [42] Sohn J W, Jeon J and Choi S-B 2013 An investigation on dynamic signals of Mfc and PvdF sensors: experimental work *Adv. Mech. Eng.* **5** 420345

- [43] Arce G A, Noorvand H, Hassan M M, Rupnow T and Dhakal N 2021 Feasibility of low fiber content PVA-ECC for jointless pavement application *Constr. Build. Mater.* **268** 121131
- [44] Lubliner J, Oliver J, Oller S and Oñate E 1989 A plastic-damage model for concrete *Int. J. Solids Struct.* **25** 299–326
- [45] Wang J, Jivkov A P, Li Q M and Engelberg D L 2020 Experimental and numerical investigation of mortar and ITZ parameters in meso-scale models of concrete *Theor. Appl. Fract. Mech.* **109** 102722
- [46] Derakhshani M, Momenzadeh N and Berfield T A 2021 Analytical and experimental study of a clamped-clamped, bistable buckled beam low-frequency PVDF vibration energy harvester *J. Sound Vib.* **497** 115937
- [47] Baumgärtel K H, Zöllner D and Krieger K-L 2016 Classification and simulation method for piezoelectric PVDF sensors *Procedia Technol.* **26** 491–8
- [48] Hou S, Zhang H B and Ou J P 2012 A PZT-based smart aggregate for compressive seismic stress monitoring *Smart Mater. Struct.* **21** 105035
- [49] Li P, Jiang W, Lu R, Yuan D, Shan J and Xiao J 2022 Design and durability of PZT/PVDF composites based on pavement perception *Constr. Build. Mater.* **323** 126621
- [50] Shirinov A V and Schomburg W K 2008 Pressure sensor from a PVDF film *Sens Actuators A* **142** 48–55
- [51] Seminara L, Capurro M, Cirillo P, Cannata G and Valle M 2011 Electromechanical characterization of piezoelectric PVDF polymer films for tactile sensors in robotics applications *Sens Actuators A* **169** 49–58